ABSTRACT

A TWO DIMENSIONAL MODEL OF MAGNETIC FIELD ASSISTED ASSEMBLY

by
Gaurav Devrani

A simplified model to simulate the magnetic field distribution for applications in magnetic field assisted assembly of semiconductor device structures, using commercial software (Vizimag), has been implemented. Solenoids have been utilized to serve as electromagnets that are responsible for the assembly process. Magnetic shielding techniques have been deployed to isolate the influence of one solenoid over another. These solenoids are used to move the devices that need to be placed in recesses within the substrate. The bottom of the devices and the recesses are coated with magnetic materials to facilitate the movement and placement of devices within the recesses in the substrate. The semiconductor devices may be made from a variety of materials such as semiconductors, to perform various functionalities.

A TWO DIMENSIONAL MODEL OF MAGNETIC FIELD ASSISTED ASSEMBLY

by
Gaurav Devrani

A Thesis
Submitted to the Faculty of
New Jersey Institute of Technology
In Partial Fulfillment of the Requirements for the Degree of
Master of Science in Electrical Engineering

Electrical and Computer Engineering Department

August 2008

APPROVAL PAGE

A TWO DIMENSIONAL MODEL OF MAGNETIC FIELD ASSISTED ASSEMBLY

Gaurav Devrani

8-25-08

Dr. N.M.Ravindra, Thesis Advisor — Date
Joint Graduate Program Director and Graduate Advisor
Physics Departments of NJIT and Rutgers-Newark

9/15/08

Dr. Walid Hubbi, Committee Member — Date
Associate Professor of Electrical and Computer Engineering, NJIT

8-25-08

Dr. Michael R. Booty, Committee Member — Date
Professor of Mathematics, NJIT

8-25-08

Dr. Anthony T. Fiory, Committee Member — Date
Research Professor, Physics Departments of NJIT and Rutgers-Newark

8-25-08

Dr. Edip Niver, Committee Member — Date
Professor of Electrical and Computer Engineering, NJIT

BIOGRAPHICAL SKETCH

Author Gaurav Devrani

Degree Master of Science

Date: August, 2008

Undergraduate and Graduate Education:

- Master of Science in Electrical Engineering,
  New Jersey Institute of Technology, Newark, NJ, August, 2008

- Bachelor of Technology in Electronics Engineering,
  Govind Bhallabh Pant Institute of Agriculture and Technology,
  Pantnagar, India, June, 2003

Major: Electrical Engineering

ACKNOWLEDGEMENT

This work would not have been completed without the help and support of many individuals. I would like to thank everyone who has helped me along the way, particularly, Dr Nuggehalli M. Ravindra who not only served as my research supervisor, but also provided support, encouragement, and reassurance. I also thank Dr. Walid Hubbi, Dr. Michael R. Booty, Dr. Anthony T. Fiory, and Dr. Edip Niver for serving on my thesis committee and providing valuable suggestions. I appreciate the work of my colleague, Shudhakar Shet, whose work has been a great help to me in developing my Thesis.

TABLE OF CONTENTS

TABLE OF CONTENTS
(Continued)

LIST OF TABLES

Table **Page**

LIST OF FIGURES

Figure **Page**

LIST OF FIGURES
(Continued)

Figure **Page**

CHAPTER 1

INTRODUCTION

This thesis presents a study of the fundamental mechanisms of magnetic field assisted assembly using a two-dimensional model. The heterogeneous integration of various devices on a single wafer is critical for performing a variety of functionalities such as lab on a chip (LOC). This ability leads to an increase in the density of chips per unit area and thus reduces the cost of the device assembly. Optoelectronic devices such as light emitting diodes, optical sensors and semiconductor lasers are made from III-V compound semiconductors which have direct band gap. This property makes them better suited for applications in optoelectronics. Silicon suffers from an indirect band gap that makes it less suitable for applications in optoelectronics. The monolithic integration of optoelectronic devices on silicon complimentary metal oxide semiconductor (CMOS) [1] circuits is beneficial for ultra high frequency communication systems. The integration of the devices is of utmost importance, but this integration has to be at the micron length scale level because of the device dimensions. The fabrication sequences and the material requirements have been hurdles in the manufacturing of such devices. The wafer–scale assembly technique which combines materials with different properties on to a single wafer can act as a better alternative for the device assembly.

Current integration strategies in the manufacturing sector are 'pick and place' [2] and 'assembly using external magnetic array' [3]. The former technique is a serial assembly, which has cost and speed constraints. The other technique uses precise magnetic field in the "magnetic arrays" along with the vibration on the substrate. Due to these

disadvantages, a newer assembly technique called "magnetic field assisted assembly" [4] was developed.

The various techniques for device integration and device bonding, being practiced currently in the semiconductor industry are described, in brief, in the following sections.

1.1 Flip Chip

A flip chip bonding approach [5] is incorporated for mounting semiconductor devices on to the final wafer. There are various flip chip bonding techniques such as Solder Bump Flip chip bonding, Stud Bump Flip Chip, Polymer Bump Flip Chip, Anisotropic Conductive Film (ACF) Flip Chip, Electroless Nickel-Gold Flip Chip, Thermosonic Flip Chip Assembly, etc. These bonding techniques are utilized according to the applications. The flip chip technique is also known as "Controlled Collapse Chip Connection".

1.1.1 Solder Bump

The solder bump [6] is a four step process: preparing the wafer for putting the solder bump, placing the solder bump, attaching the die with the substrate, sticking the adhesive on to the assembly.

1.1.2 Stud Bump

For stud bump flip chip assembly [7], gold is on the die bond pads, which is then connected to the substrate with an adhesive. This does not require wafer processing, as

they can be wire bonded. The layer of the adhesive has to be controlled and there has to be linearity in all the bumps.

This bumping technique can de done on a wire bonder. This implies that it does not require a full wafer; the die can be flipped without any processing. This makes bump quick and supple for production.

1.1.3 Polymer Bump

The polymer bump process [8] is one in which isotropically conductive, silver filled polymers are stencil printed through metal stencils to form polymer bumps on the wafer which covers the aluminum bond pads of the devices.

The polymer flip chip process combines exactness and stencil printing techniques with highly conductive and isotropic, conductive polymers. The polymers are either thermo set, which does not deform with heat, or thermoplastic, which softens with heat. These printing steps are performed through laser etched or electroformed metal stencils.

1.2 Fluidic Self Assembly

Fluidic self-assembly (FSA) [9] is a technique that integrates different devices of dissimilar materials and processes. This integration is performed by fluidic transportation of different sizes of blocks or devices on to similar holes that are made in the substrate wafer.

An example of such a kind of process comprises placing GaAs devices on a silicon wafer is shown in Figure 1.1. GaAs devices are grown on GaAs substrates using

molecular beam epitaxy (MBE). A sacrificial layer of AlAs is grown on the device. The device formed is then truncated into pyramidal shapes using ion-milling and photolithography. These devices are then released from the substrate by etching the sacrificial layer with hydrofluoric acid. These devices are now moved by ethanol to be finally dispersed on to silicon receptor substrate, where they are placed into recesses formed by potassium hydroxide (KOH) etching.

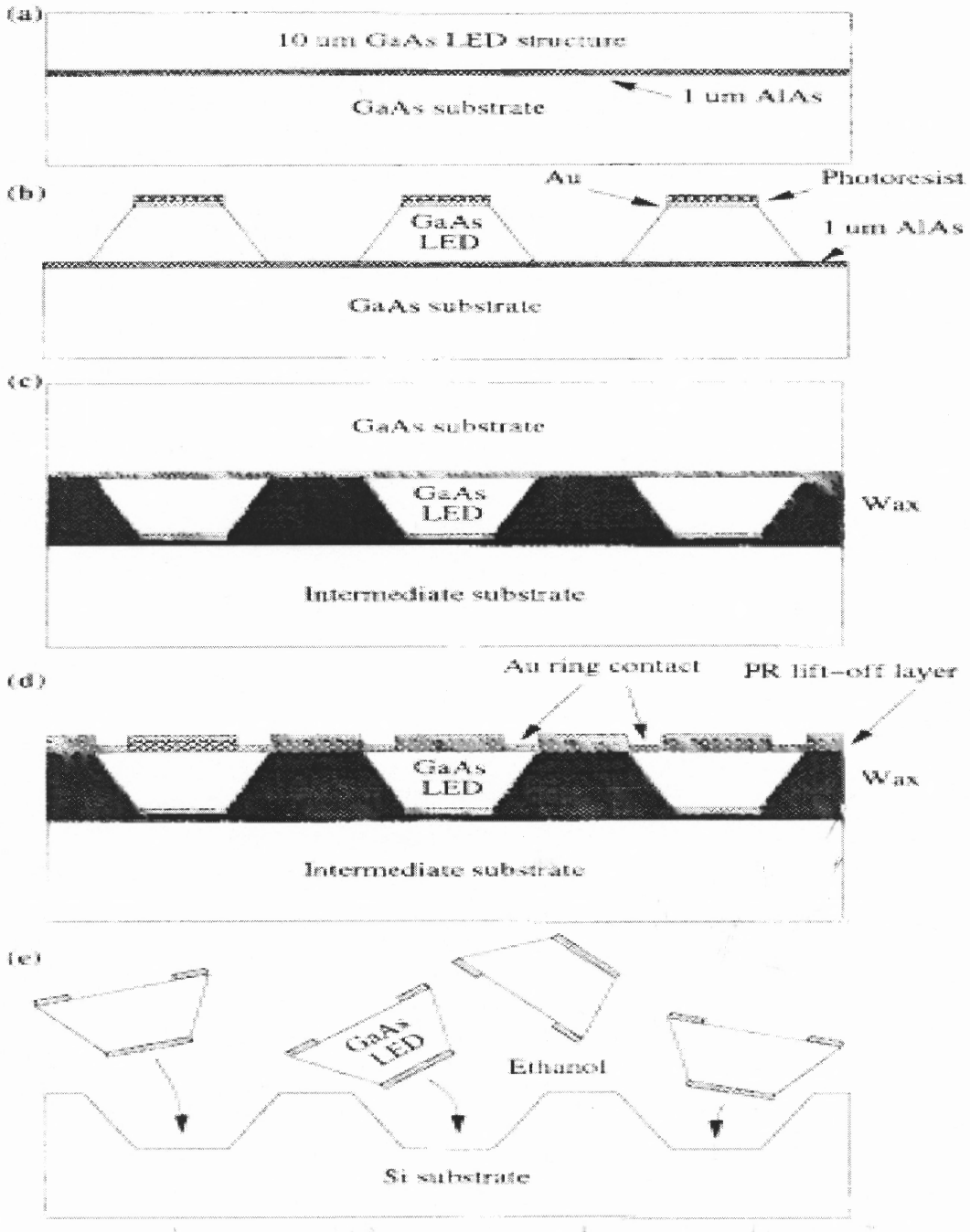

Figure 1.1 Schematic of the fluid self-assembly process: (a) MBE grown structure with 1 μm AlAs etch-stop layer, (b) trapezoidal GaAs mesa definition, (e) bonding to intermediate substrate with wax, (d) top-side ring contact metallization, (e) solution containing the GaAs blocks dispensed over patterned Si substrate and Si substrate with GaAs, light-emitting diodes integrated by fluidic self-assembly. [9]

The efficiency of the FSA technique is determined by the ability of the assembly process to place devices at the desired recesses in the wafer. There are several factors which will affect how productively the devices can be made to fill recesses.

One important variable is the number of blocks (or devices) involved in the process; the greater the number of blocks, the greater the fill ratio. A second important factor is the liquid used to perform the fluidic transport. The liquid used in transportation plays a vital role, as the forces between the wafer and the liquid and the devices and the fluid have to be taken into consideration. The fluid also reduces the force between solid objects, resulting in better block mobility across the surface of the substrate. The viscosity of the liquid can affect how blocks move through it on their way to the substrate. The first choice would be water; however, Si is hydrophobic, resulting in a tendency of blocks to float on the surface of water. This effect was not significant in the case of the large blocks which, because of their large mass, were observed to precipitate through the water. For this reason, water was used to perform FSA experiments, but methanol is also used as Si is not phobic to methanol. Finally, in the most ideal conditions, not all blocks are able to fill a hole (recess) during a single pass across the substrate surface. Moreover, not all of the holes in a substrate pattern are filled by a single pass of blocks over it. The efficiency of the process would therefore be greatly enhanced by continuous recirculation of blocks which have not filled a hole during a given pass. Thus, there are ways in which we can reprocess those devices. For example, this can be accomplished by using the "bubble pump" apparatus shown in Figure 1.2.

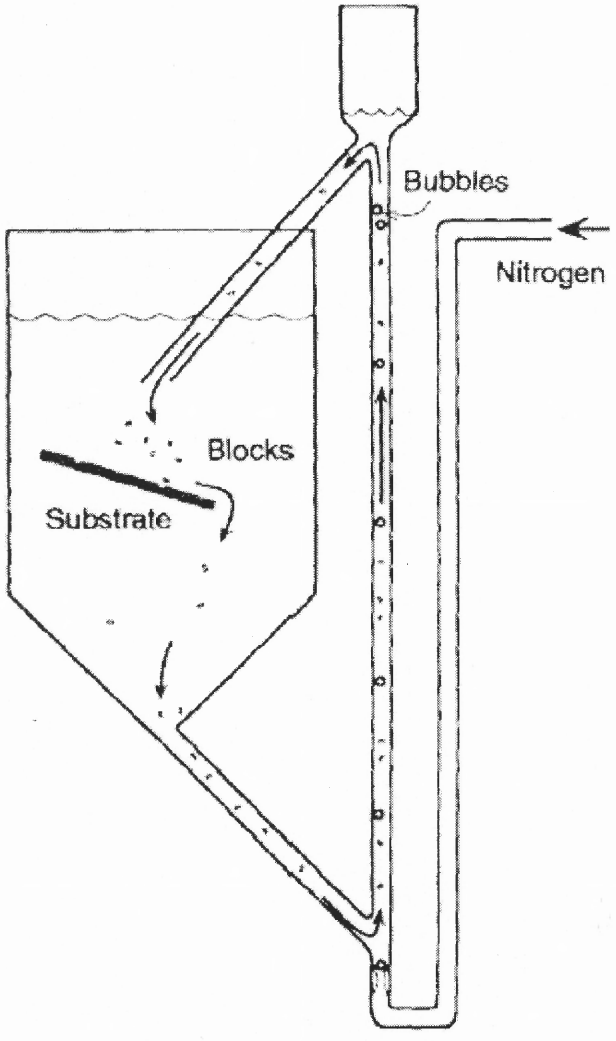

Figure 1.2 A schematic of the bubble pump apparatus for block recirculation. The substrate is placed beneath the output spout at the top of the apparatus. [10]

The principle of operation of this apparatus is quite simple: nitrogen gas bubbles are introduced into the column on the right of the figure, causing an upward fluid flow which carries blocks that are then collected at the bottom of the apparatus and brought back up to the top. The rate of recirculation can be controlled by the nitrogen pressure.

Each successive pass of blocks across the substrate surface is expected to increase the percentage of filled holes.

1.3 Advantages of Fluidic Self Assembly

The fluidic self-assembly integration [11] has many advantages over other integration techniques such as hetero epitaxial growth and wafer bonding. A large number of devices (optical, optoelectronic etc.) can be placed on a single silicon wafer. However, with techniques such as epitaxial lift-off, the entire GaAs wafer area must be used to fabricate these devices. Since only a small fraction of the wafer area is used, much of the expensive grown wafer is wasted.

Fluidic self-assembly allows the fabrication of GaAs devices, as densely packed as possible, on the grown wafer to maximize the wafer area. Approximately 3 million devices can be made from a two inch diameter GaAs wafer. Blocks can be dispensed over many Si wafers, because the unused blocks may be recycled. This gives greater flexibility to the integration process because the GaAs devices and Si circuitry can be processed separately prior to self-assembly.

1.4 Magnetically Assisted Statistical Assembly (MASA)

Magnetic Assisted Statistical Assembly (MASA) [12] is the heterogeneous integration of semiconductors, which can be used to integrate optoelectronic devices such as laser diodes that are made from a variety of semiconductor materials on a silicon wafer.

This technique uses statistical self-assembly to locate compound semiconductor device heterostructures in shallow recesses that are patterned into the surface of an

integrated circuit wafer, and short-range magnetic attractive forces to retain them. When all of the recesses on the wafer are filled with heterostructures, the wafer is processed further to transform the heterostructures into devices that are monolithically integrated with the underlying circuitry. The process is summarized in Figure 1.3.

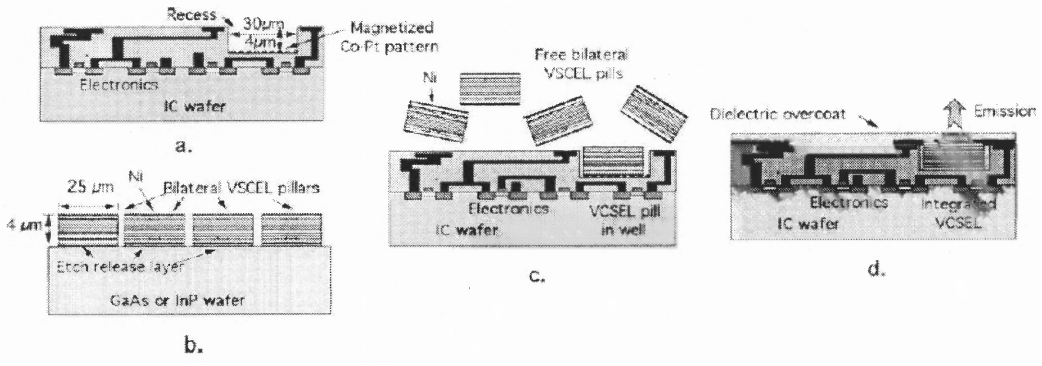

Figure 1.3 The MASA process. (a) The processed IC wafer with prepared recesses. (b) The p-side down VCSEL wafer with pillars etched in a close-packed array. (c) Statistical assembly of freed nanopills into the recesses on the IC wafer. (d) After completion of device processing and integration. [13]

During statistical assembly, the surface of a wafer prepared with recesses will be flooded with several orders of magnitude more nanopills than are needed to fill its recesses. The large number of pills will mean that there are many pills in the vicinity of each of the recesses, and the highly symmetric nature of the pills and recesses will result in a high probability that a pill in the vicinity of a recess will fall into it. The strong short-range magnetic attractive force which will come into play when a pill settles into a recess will keep the pill from being removed from the recess by gravity or by another nanopill or by the fluid used to flood the surface with nanopills. The process can be favorably

compared to carrier trapping by deep levels in semiconductors, and the probability that a given recess is filled will be one. Once the nanopills are assembled on the circuit wafer, they will be fixed in position using a polymer which will also fill in any voids on the surface surrounding the pills and planarize the surface. The complete process consists of formation of heterostructures and integrating them with the underlying electronics by standard monolithic photolithographic processes. The MASA process is an attempt to combine the best features of the Epitaxy-On-Electronics (EoE) and Aligned Pillar Bonding (APB) integration techniques, with the ability to monolithically integrate any semiconductor device on any substrate.

1.5 Direct Epitaxy

This is a technique [14] in which monolithic layers of material are grown over silicon substrate by using Molecular Beam Epitaxy (MBE). Due to the stress and strain between layers of different materials, there is a mismatch between the lattices that results in poor performance of the device. Using a thick buffer layer can alleviate the device performance but there is still a need to maintain low growth rate temperature; temperature of the subsequent processing steps is also limited to low values.

1.6 Assembly using External Field

This approach [15] is similar to all the other approaches; here also microcomponents are assembled on the substrate. The method uses "master array" [15], a structure that is made of an array of magnetic potential wells. The magnetic field applied to the receptor sites on the substrate is external and is focused. This mechanism, shown in Fig. 1.4 (a), can place

only one component at a time. Therefore, there has to be parallel processing for many such units. The figure shows a magnetic assembly setup with one magnet and one chip. The system consists of the following: a master array in which high aspect ratio neodymium iron boron NdFeB magnets are embedded; Figure 1.4 (b) shows the cumulative pattern of the same array. The target chips have a coating of soft magnetic material CoNiP (1μm), that is prepared using electrolysis plating method. This approach consists of a vibration system which allows the distribution of the chips over the surface of the substrate and discards misaligned chips during the assembly process.

During the process, there is a large number of chips that are randomly distributed on the host substrate and when there is a vibration in the table on which they are placed, each chip will move until they are stochastically placed in the cavity or the recess of the substrate. They are trapped in the cavity because of the magnetic field generated by a corresponding magnet underneath. The magnetic coating on each chip will get magnetized by the corresponding magnetism due to the master array and, therefore, a force of attraction is developed between the master array and the chip which results in placing the chip in the recess, with magnetic coating facing inside the recess and the circuit facing up. There has to be a match between the dimension of the recess and the chip. After the assembly process is performed, the chip is attached by wire bonding or flips chip bonding.

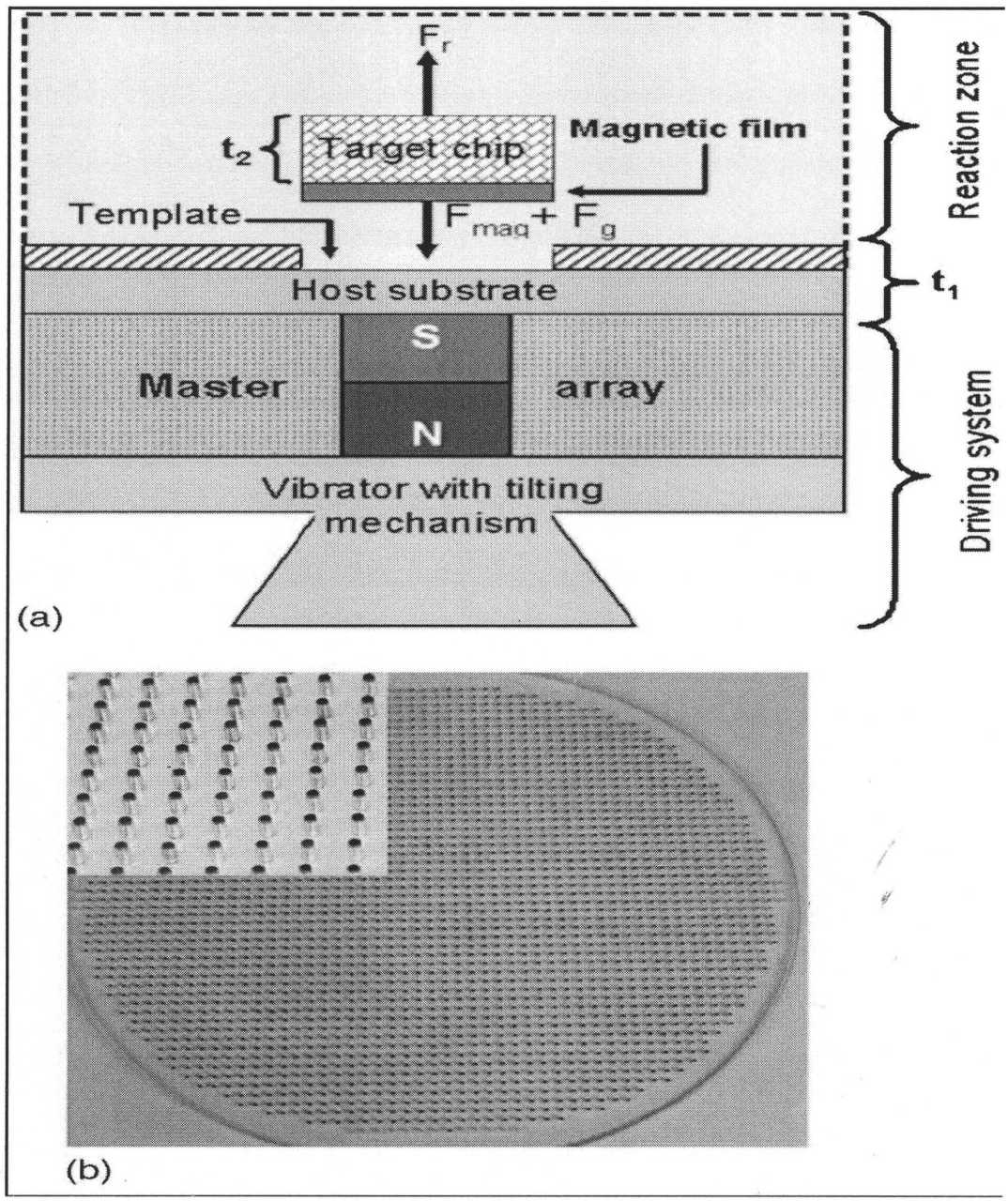

Figure 1.4 (a) A cross-sectional view of the assembly setup; **(b)** magnet array of 2500 NdFeB magnets (1 x 4 mm^2) embedded in acrylic substrate (8 inches in diameter). [15]

As the chips fluctuate on the substrate, they can land in four different ways on to the recess. The analysis of these four positions is shown below in Figure 1.5:

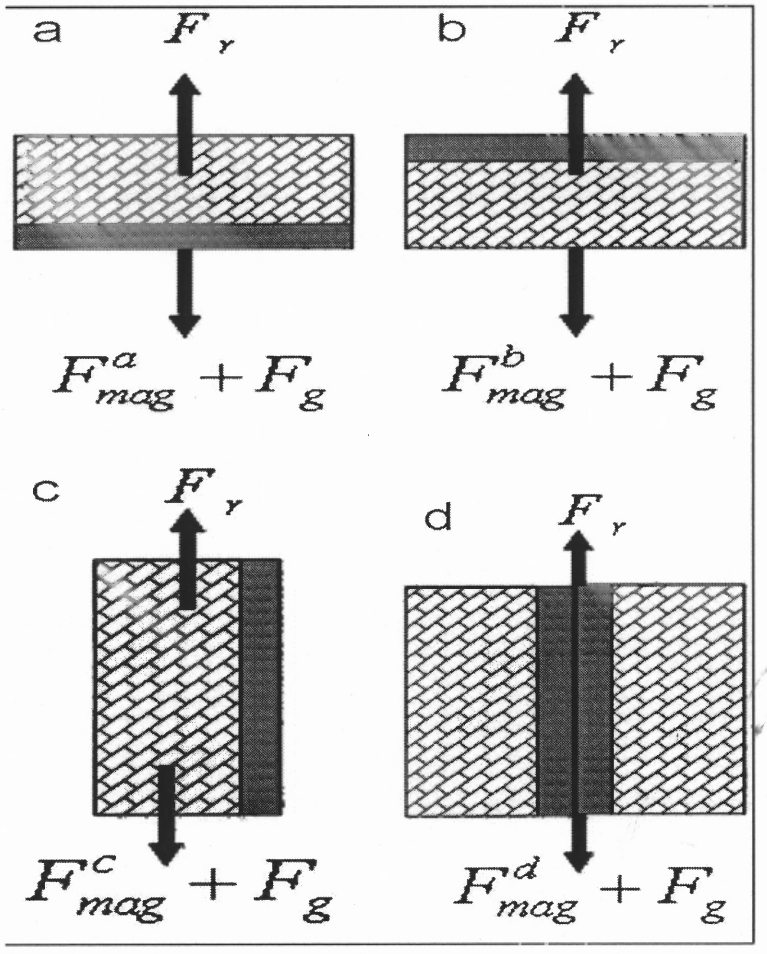

Figure 1.5 Position of the chips on the host substrate: a) magnetic film down, b) magnetic film up, c) perpendicular position, and d) chip-chip chaining. [15]

Magnetic coating down - Figure1.5 (a): The position of the chip is in such a way that the magnetic film is facing down in the recess. In this scenario, $F_{mag} + F_g > F_r$ condition is met, where F_{mag} is the magnetic force on the chip and the notation *a* refers to

the magnetic force in this position, F_g is the gravitational force, and F_r is the rejection force caused by the vibration of the table. The magnetic force on the chip in this configuration will be a maximum because the chip is separated only by a distance t_1 which is the thickness of the substrate.

Magnetic film up - Figure 1.5 (b): The chip is placed in such a way that the magnetic strip is facing up. In this configuration, the magnetic force is less than that in the previous scenario; the reason is, now, the chip has larger gap and that is equal to (t_1+t_2), which is the total thickness of the substrate (t_1) and the chip itself (t_2). In this case, the chip is trapped for a very short time and is rejected, due to vibrations and this condition is met when $F_{mag}+F_g<F_r$. The amplitude of the vibration plays an important role, as it has to be optimized in such a way that the attraction force $F_{mag}+F_g$ has to be greater than the rejection force F_r and the desired condition is achieved.

Perpendicular position - Figure 1.5(c): The position of the chip is now on its short axis. In this position, the chip is mechanically unstable, and because of vibrations, it attains any of the above two positions.

During chip-chip chaining, the dipole interaction between the chips causes the chip to attract to one another as shown in Figure 1.5(d). The vibration of the substrate causes the chips to knock and as they fly, they get demagnetized and detach from one another and the chip will reside in any of the first two positions (Figure 1.5 (a) and 1.5 (b)), and finally in the first position.

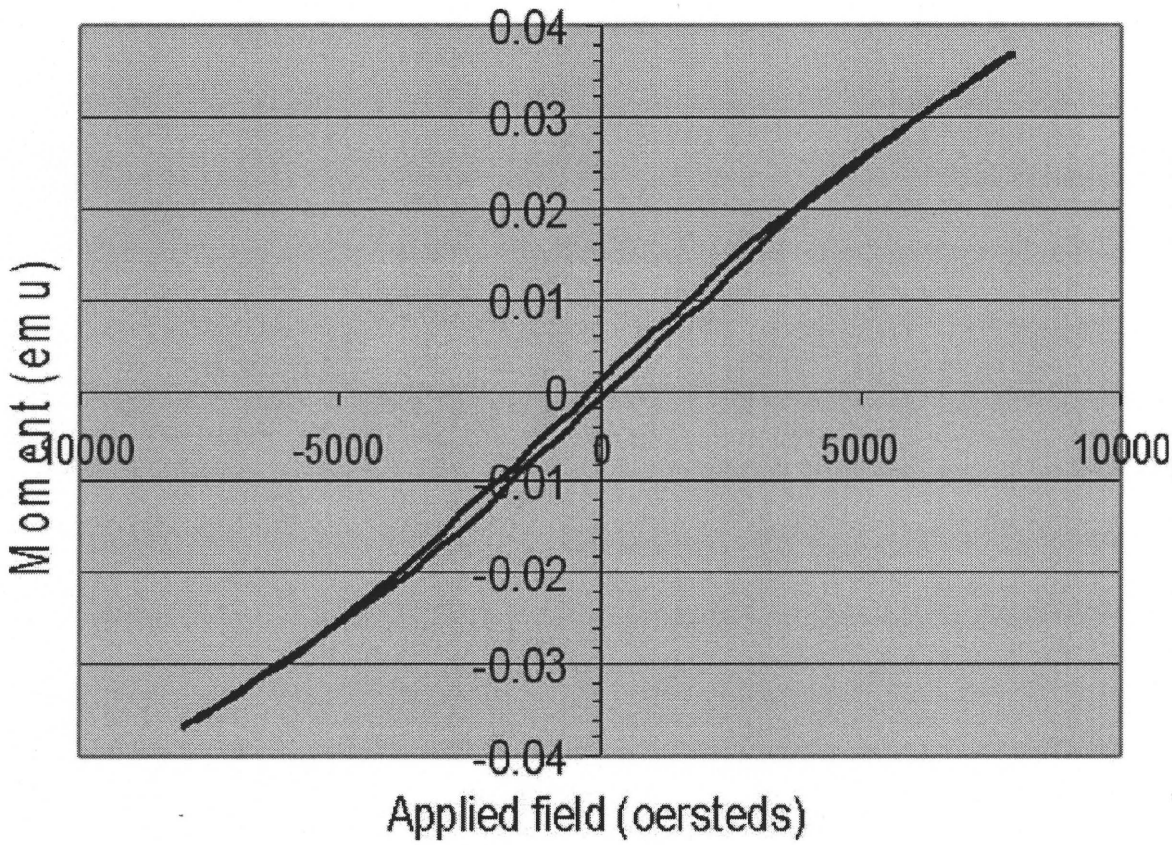

Figure 1.6 Hysteresis loop for CoNiP ternary alloy measured by vibrating sample magnetometer. [15]

In the above approach, in a soft magnetic layer of CoNiP, with coercivity H_c of 43.5 G and magnetization of M_s of 95.5 emu/g is used underneath the chip. The vibration on the table is 90 Hz which is sufficient for the chip to finally reside on the wafer as in case 1.

The 500μm thick chip is coated with 1μm film of CoNiP. A finite element analysis software, VECTORFIELDS/TOSCA, is used to evaluate the magnetic force on the chip. The NdFeB magnet and the CoNiP film coercivities are 11,000 and 8,100, respectively. The weight of a silicon chip with size of 1x1x0.5 mm is 15.3 mN. Figure

1.6 shows the simulated magnetic force generated by a 1 mm thick NdFeB magnet. In order to investigate the system capability to distinguish between the two positions, i.e., magnetic film up and magnetic film down, chips with different thicknesses ranging from 200 to 500 μm were tested. It was observed that the system can distinguish the two positions with chip thickness of 350 μm and random chip vertical alignment was observed when the chip thickness was reduced to 200 μm. Figure 1.7 (a) describes the magnetic forces experienced by the chip at various positions of the chip. Figure 1.7 (b) shows the magnetic flux density distribution along the lines described above. The magnetic flux in between each pair of magnets decreases sharply which permits to release the chips at the undesired location in the intercavity spacing by the vibration.

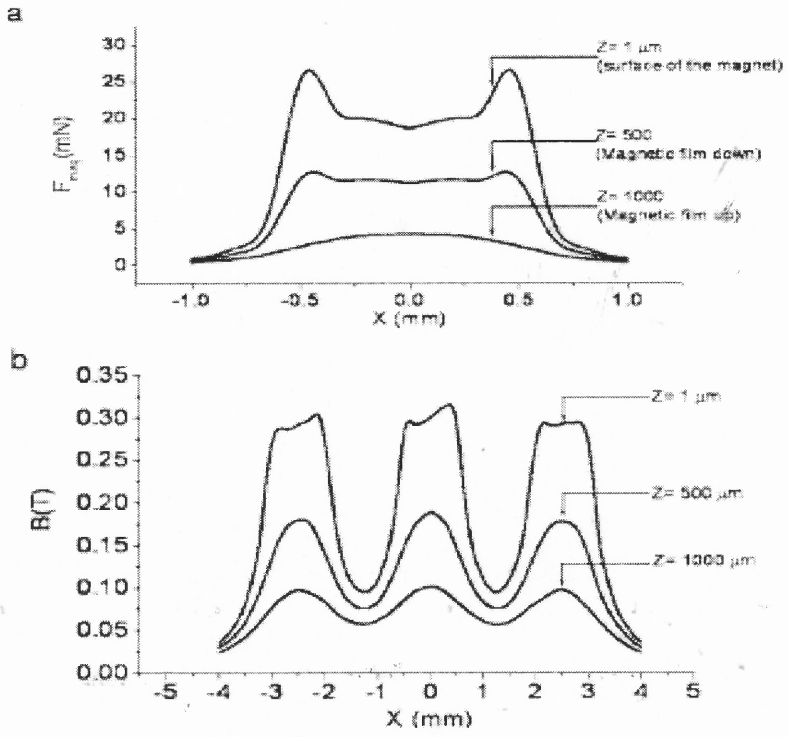

Figure 1.7 (a) Magnetic forces generated by the magnet on the chip having a magnetic film. (b) The magnetic flux distribution. [15]

CHAPTER 2

MIT MODEL

For optimal performance of optoelectronic integrated circuits (OEICs), it is imperative that silicon very large scale integration (VLSI) technology must be integrated with optoelectronic devices and circuits. This integration can be achieved by several methods; these include growth at the materials level, bonding at the device or the circuit level, etc. The group at MIT proposed Magnetic Assisted Statistical Assembly (MASA) as an approach for integration of a variety of devices and circuits. In the following section, the mathematical approach to MASA is described.

2.1 Magnetic Assisted Statistical Assembly --- Simulation

The approach to modeling of MASA, at MIT, deploys a program called ATLAS [14]. The group at MIT has simulated electrical and optical properties of p-i-n diode. ATLAS [16] is a two dimensional simulator for analyzing various device properties. The software operates on a command language, such as C and C++, wherein a mesh is created with horizontal and vertical lines and desired materials such as GaAs, InGaAs, etc., are filled in between them; even the doping profile can be handled in these regions, and the last step would be to specify the electrodes in the specific regions.

2.2 Magnetic Assisted Field Assembly

The physical simulation domain of a p-i-n photodiode is defined in a two dimensional mesh [12, 17]. For numerical accuracy, a finer mesh is made around the original mesh. In order to obtain a faster simulation, the mesh is defined to be coarser in regions away from the intrinsic region. The mesh is rectangular and the dimensions are 30 μm in length and 6.35μm in height. The width of the device is considered by a scaling factor, which is multiplied with the current obtained from device simulation.

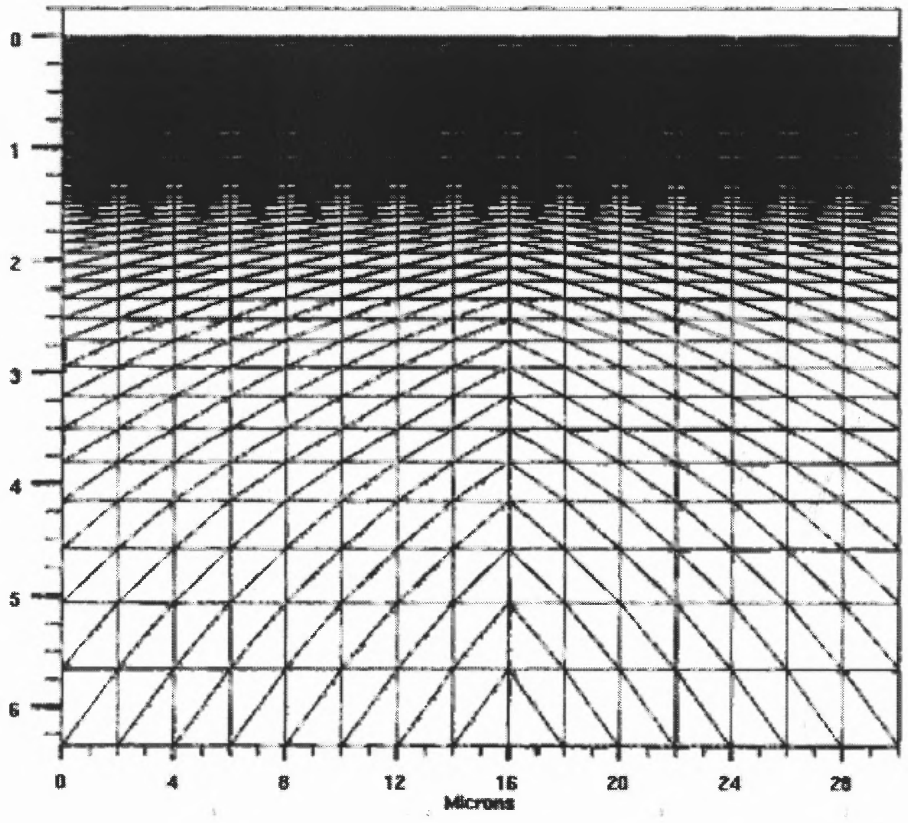

Figure 2.1 ATLAS [16] mesh structure of P-I-N photo detector.

Every part of the mesh is filled with a particular type of material. If we consider a p-i-n diode, as in Figure 2.1, the material would be InP or InGaAs. The doping concentration is $5x10^{18}$ cm^{-3} for the saturated region and the $5x10^{15}cm^{-3}$ for the intrinsic region. The concentration has to be uniform throughout the specific regions. There are two electrodes that have a ring structure that are placed on the top surface of the mesh. These are actually joined together to form the photodiode. The contact resistance is defined by the software (ATLAS).

In case of heterojunction materials, there is a difference between the band gap energies of the two materials, which creates discontinuities in the valence and conduction bands. The charge movement in the valance band and the conduction band is hindered because of the discontinuities in the bands. The valence band discontinuities are taken into account for the p-i-n heterojunction by specifying the part of the band gap difference that would be shown in the conduction band discontinuity. As far as the simulation is concerned, the conduction band gap offset is created by adjusting the electron affinity of the material on one side of the junction [1]. This is shown in Figure 2.2.

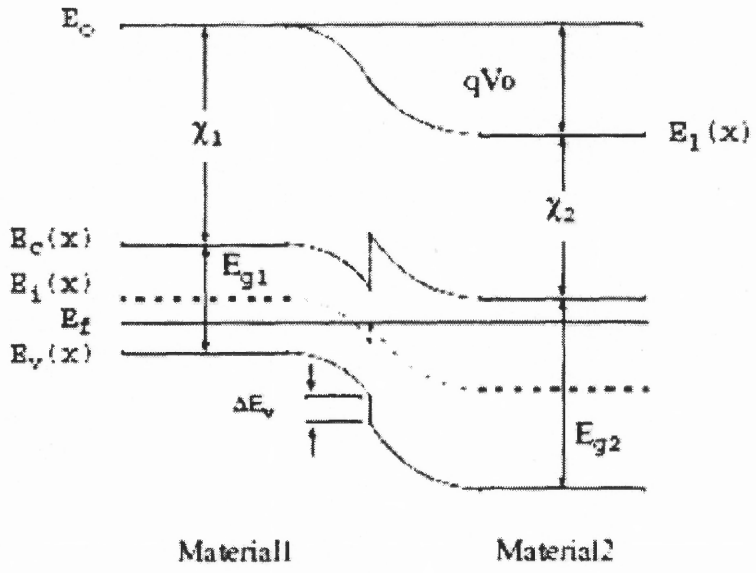

Figure 2.2 Energy band diagram of PN hetrojunction [29]

The material considered here is InGaAs or InP with the assumption that 43% band gap is assigned to the conduction band discontinuity. A diagram of a p-i-n heterojunction under zero basing condition is shown in Figure 2.3. On the left side of the diagram is the n type region and on the right side is the p type region; the intrinsic region lies in the middle of the two layers.

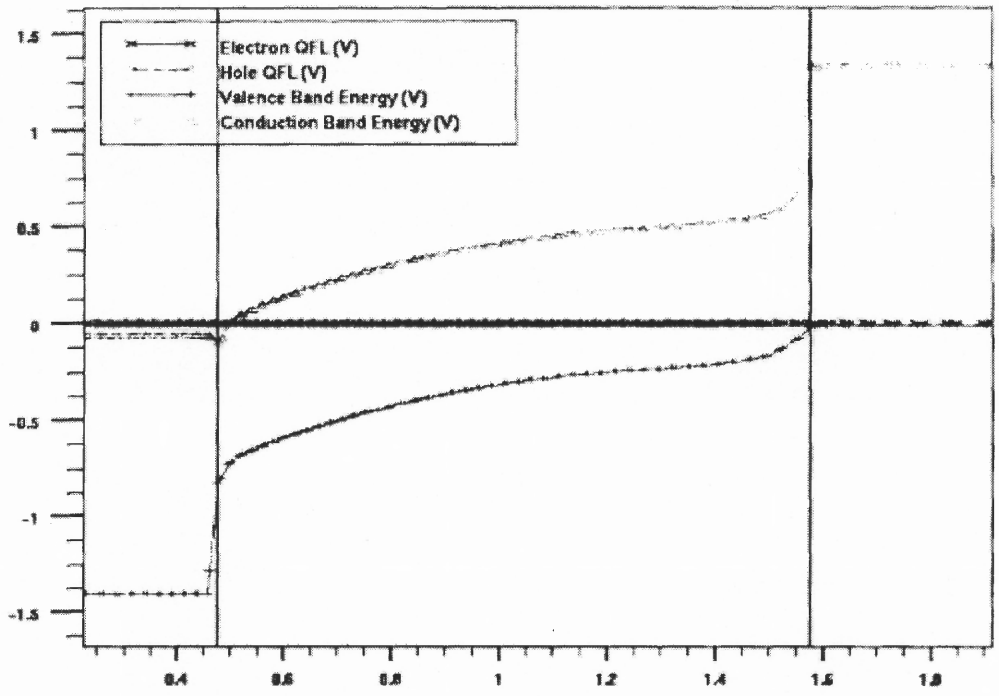

Figure 2.3 Energy band diagram at thermal equilibrium of a p-i-n diode [19]

The diagram shown below in Figure 2.4 is an energy band diagram with reverse bias of 1 volt. At the depletion layer, the charge is accumulated by a large electric field. Thus the carrier generated would sweep into the buffer region and to the contacts. The movement of quasi Fermi level due to concentration of the carriers from equilibrium is distinct in the intrinsic region.

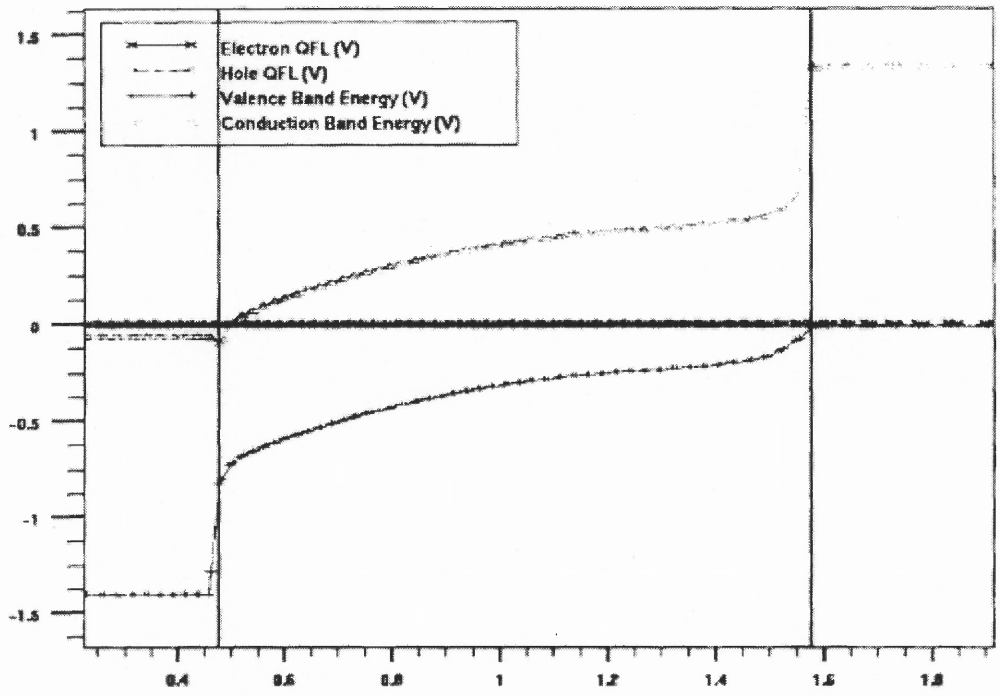

Figure 2.4 Energy Band diagram of a p-i-n photo diode under reverse bias [19]

2.3 Electrical Property

All these physical models run on ATLAS [16] (software) by employing mesh structure. The material (InGaAs/InP) and the band structural parameters will remain the same as described above. The basis of the simulation is the Poisson's equation, the continuity equation and the transport equation. The device simulation [20] is performed by using all of them at each point of the mesh, taking into consideration the boundary condition from the adjacent mesh points. The figure shown below, in Figure 2.5, is the DC sweep simulation of the photo diode. Device measurements yield dark current of $5x10^{-13}$ Amps and turn–on voltage of 0.7V.

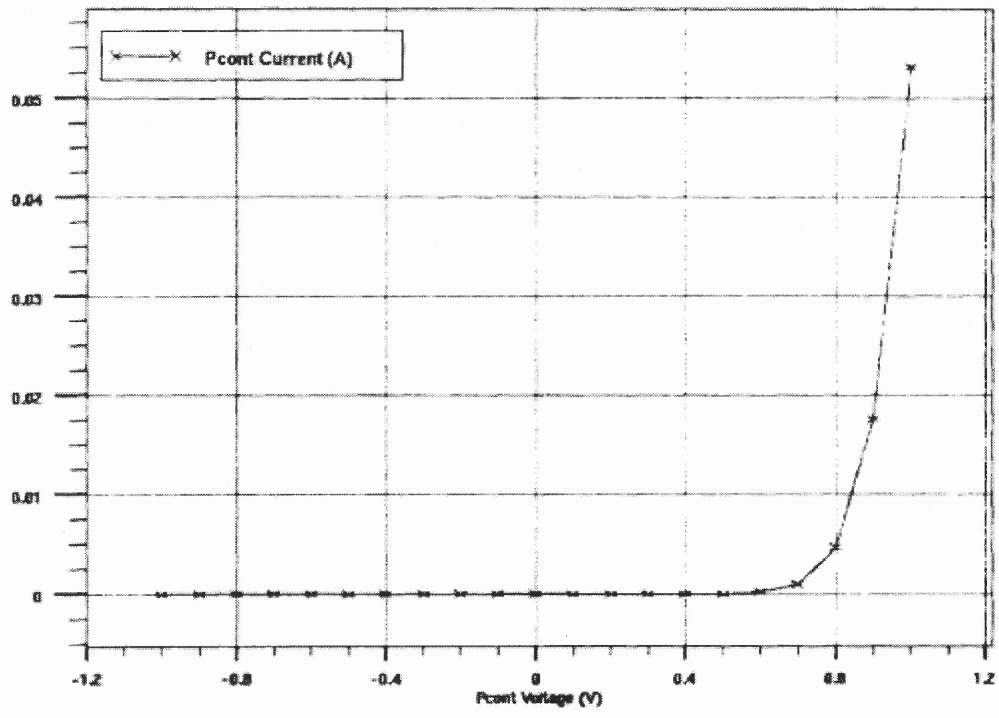

Figure 2.5 Current voltage characteristic of a p-i-n photodiode [19]

In the p-i-n photodiode, the capacitance can be calculated by considering AC small signal simulation. In the reverse bias condition, the charge is accumulated near the depletion region; thus the dominant capacitance is expected to be high in that region and is given by:

$$C=\varepsilon A/d \qquad (2.1)$$

Where, d is the thickness of the intrinsic region, A is the area of the photo diode and ε is the dielectric constant. If the intrinsic region thickness is 1.1μm, and the area is 900μm^2, the photodiode capacitance is 108 fF. This result matches with the AC small signal simulations. Thus the capacitance of the photodiode at 1 GHz can be extracted.

2.4 Optical Property

ATLAS uses LUMINOUS, a ray-optics based program for optical analyses and simulation [21]. The device simulator calculates optical intensity profiles in the semiconductor and converts into photogeneration rates. Optical simulation, in general, is divided into two parts - real and imaginary. The real component of the refractive index within optical ray yields optical intensity profiles of the device. The imaginary part of the refractive index calculates the carrier concentration at each point in the mesh.

The photogeneration rate at each grid of each mesh is calculated by the influence of the properties of the optical ray and these properties are light absorption, light reflection and light transmission. The photocurrent, optical frequency and transient response can be extracted from this information.

A single ray of light of wavelength 1μm and above is termed as the light source. The ray enters with a single wavelength (1550 nm) and optical intensity of $1W/cm^2$ in the entire width of the device. Reflection is considered only from the top of the device by considering the real part of the refractive index to obtain the transmitted and the reflected component of the incident ray.

From the current voltage measurements, a current of 7.5mA is considered for reverse bias conditions. In Figure 2.6, the current voltage characteristics are shown for a device under illumination. In reverse bias, the current increases due to the photo generation in the depletion region.

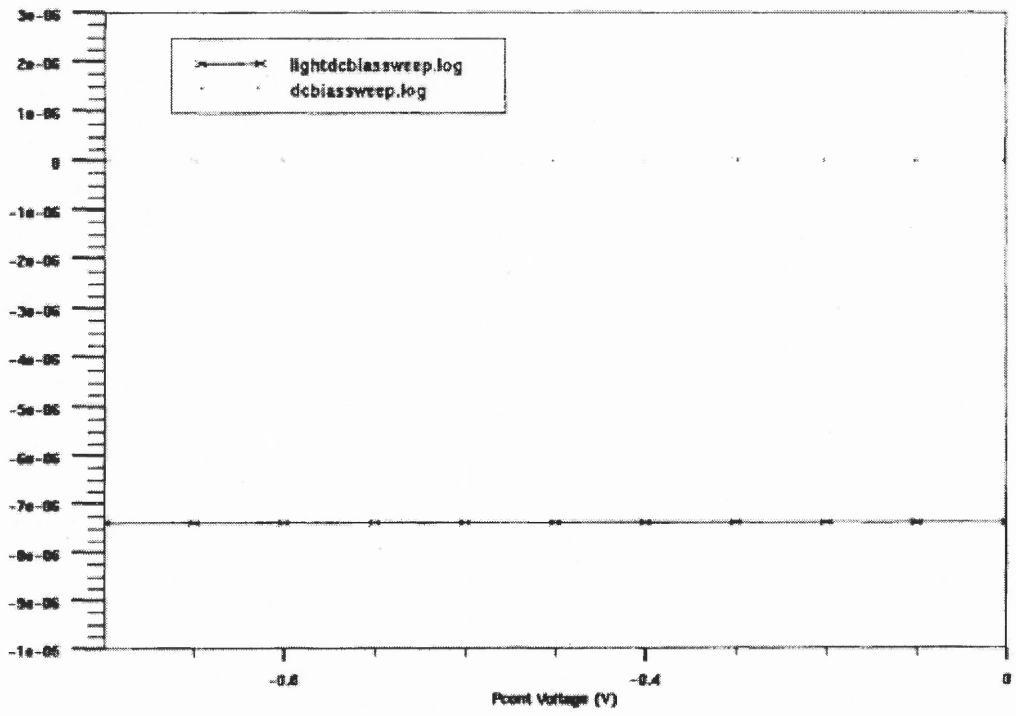

Figure 2.6 DC photo current for p-i-n diode [19]

The quantum efficiency is the ratio of the measured photocurrent to the source photocurrent. ATLAS output would readily yield source photocurrent; for this photodiode, it is 11.22μA, which yields a quantum efficiency of 66%. If we compare it with silicon based photodiodes (4-5%), this quantum efficiency is very high.

As can be seen in Figure 2.7, the intrinsic cut-off frequency of the photodiode is 4.5GHz at 500 ohm load resistance. This frequency has been calculated by using an AC optical source simulator.

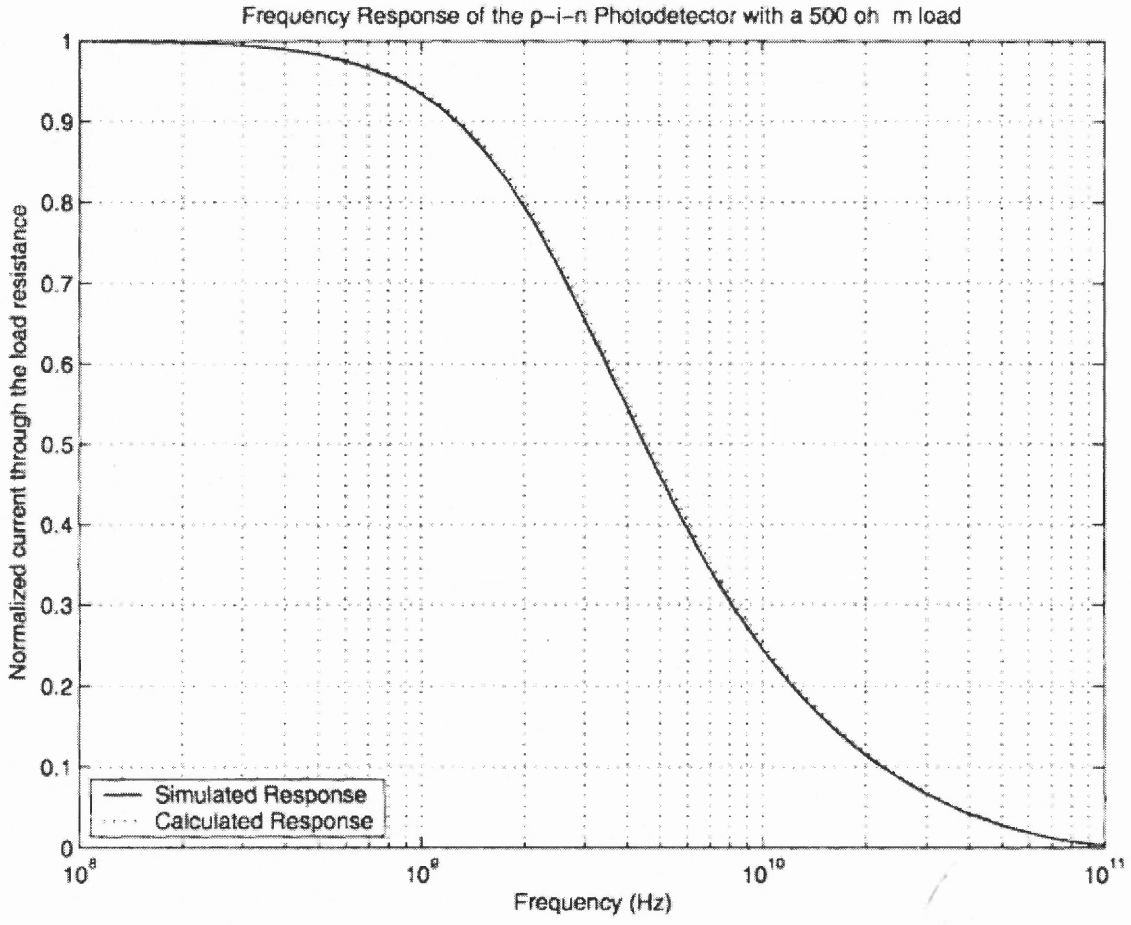

Figure 2.7 Optical frequency response of a p-i-n diode [19]

The last step is the transient characteristic of the photo diode. The optical square wave input source will yield an output which shows rise and fall times of the current. The optical transient response is shown in Figure 2.8. The simulated input light source has 50% duty cycle. It is shown in the upper half of the figure. In the lower half, the output is shown when the input is applied across the 500 ohm resistor. The output of the photodiode has a rise and fall times of 100ps.

The cut off frequency (f_{3dB}) is:

$$f_{3dB}=t_d/2JIt_r \tag{2.2}$$

where, t_r is the rise time and t_d has a value of 2.8 ns. This has been obtained by using Fourier transform and it is in accord with 4/5 GHz cut off frequency and 100ps rise and fall times.

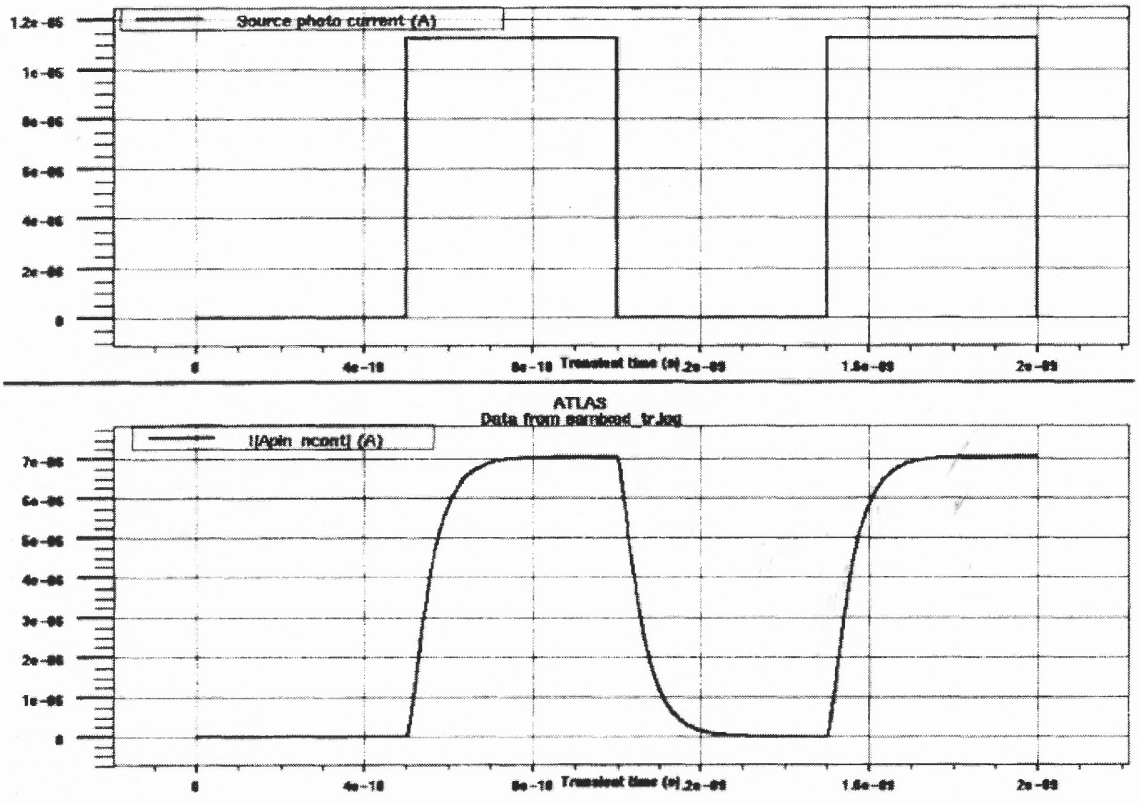

Figure 2.8 Optical transient response of a p-i-n diode: the top plot shows the source photo current and the bottom plot shows the output current of the photo diode in response to the optical input. [19]

CHAPTER 3

FLUIDIC ASSEMBLY

3.1 Introduction

For the fabrication of high performance electronics devices, we utilize hetrojunction integration [1] of microelectromechanical devices (MEMS) [18] and optoelectronic devices [22] on to the same substrate. Optoelectronic devices such as light emitting diodes and photo detectors are generally made of III-V compound semiconductors; they have direct band gap. Unlike silicon which has an indirect bandgap, these materials have direct bandgap which makes them suitable for optoelectronics.

Today, in semiconductor manufacturing, the device integration technology works on "pick and place" [13] serial assembly technique, which is expensive and is a tedious job, as the robot has to pick a large number of micron scale components and place it on to the wafer at the desired location. This requires great precision and control. During the process, it is required to take care of all the small adhesive and cohesive forces between the devices and the devices and the tools. The pick and place technique requires a large clean room; this combined with the need for the robot makes it expensive.

3.2 A Model for Field Assisted Fluidic Assembly

The location of the device relative to the recess in the substrate is important as we need to manipulate the magnetic field in order to place the device at the desired location. The model for magnetic field assisted fluidic assembly [23] describes such a situation and yields quantitative results. The movement of the device is controlled by gravitational

force in the vertical direction and by electromagnetic field in the horizontal and vertical direction; the vertical fields are developed by permanent magnets. The model assumes that the objects are small enough so that their size and orientation are unimportant and that they have a controllable charge to mass ratio. The initial conditions for the objects are:

(0, 0, z) for position,

(0, 0, 0) for velocity,

z is the initial height measured above the xy-plane of the substrate.

In this model, the velocity and position is governed by the resultant of the electromagnetic, gravitational and drag forces.

Here, the electric field is confined to two dimensions, i.e., the xy-plane ($\mathbf{E} = E_x\mathbf{i} + E_y\mathbf{j}$) and the magnetic field is confined to the z-axis ($\mathbf{B} = B_z\mathbf{k}$). This configuration has been intentionally chosen so that the gravity and drag acts in z direction and the horizontal motion (xy plane) is controlled by the electronic and the magnetic forces, as these forces would not affect the fall of an object inside the wafer.

The time taken by the object to reach the recess, in the z direction, which is not affected by the electromagnetic force, is:

$$T_f = (2z/g)^{0.5} \qquad (3.1)$$

The value of time (T_f) can only change by the influence of drag. For this value of T_f, a constant value of magnetic field could be developed and, therefore, a relationship between the final position (x, y, 0) value and the electric field is derived. This can be concluded from this that, if we know the initial position (0, 0, z) and under a constant

magnetic field, the object can be placed at any final position (x, y, 0) by adjusting the electric field according to the relation found below.

The model uses the Lorentz force that is acting on a charged particle to give the equation of motion:

$$m\mathbf{a}=m\mathbf{g}+k\mathbf{v}+e\mathbf{E} + e(\mathbf{v} \times \mathbf{B}) \quad (3.2)$$

Where, $\mathbf{g} = -g_k$, $E = E_x\mathbf{i} + E_y\mathbf{j}$, $B = B_z\mathbf{k}$, k is the drag coefficient, and m and e are the object's mass and electric charge, respectively.

The model uses the following parameterized variables:

$r' = r/z$ the parameterized dynamical variables (3.3)

$v' = v / z$ (where z is the height in the initial position (0, 0, z)

$a' = a / z$ and η is defined below)

$a'' = a'/|\eta|$

$G= (1/z)(g)(1/|\eta|)$, the augmented gravitational field (3.4)

$\beta_x = (1/z)(e/m)(E_x/|\eta|)$ the augmented electric field in the x-direction

$\beta_y = (1/z)(e/m)(E_y/|\eta|)$ the augmented electric field in the y-direction

$\eta = (e/m)B_z$, the augmented magnetic field in the z-direction

$\zeta = \eta /|\eta|$, a parameter that preserves the sign of the magnetic field

$T = (k/m) (1/|\eta|)$ the augmented drag-force constant

The parameterized differential equation, including the drag force, in component form is:

$$a''_x = Tv'_x + \beta_x + \zeta v'_y$$

$$a''_y = Tv'_y + \beta_y - \zeta v'_x$$

$$a''_z = G + Tv'_z$$

The parameterized differential equation without drag (T = 0) in component form is:

$$a''_x=\beta_x + \zeta V'_y \qquad (3.5)$$

$$a''_y = \beta_y - \zeta V'_x$$

$$a''_z = G$$

The initial conditions are r'(t=0) = (0, 0, 1) and v'' (t=0) = (0, 0, 0).

The differential equations (3.5) can be solved analytically and expressions for the fields that give a final position (x', y', 0) of the object at time T_f are:

$$\beta_x = |\zeta|(A_x' - B_y')/(A_2 + B_2) \qquad (3.6)$$

$$\beta_y = |\zeta|(B_x' + A_y')/(A_2 + B_2)$$

Where, $\varphi = |\zeta| T_f$, $A = 1 - \cos\varphi$ and $B = \varphi - \sin\varphi$. Note that the solutions for β_x and β_y are linear functions of x' and y'.

The solution of equations (3.4), which include the influence of drag, can also be found, and the expressions for the fields as functions of x' and y' are formally the same as (3.6), but now,

$$\varphi=|\eta| T_{fn} \qquad (3.7)$$

$A = 1 - \cos\varphi - \zeta T\sin\varphi + |\eta|TT_{fn}$ and

$B = \varphi - \sin\varphi + \zeta T\cos\varphi - \zeta T + \frac{1}{2}\eta |\eta|TT_{fn}$

Here $T_{fn} = T_f + \sigma$, and σ is the n^{th} order correction of the time of flight modified to include the drag-force.

The parameter φ is proportional to η, with T_f being a constant determined by the initial height. For practical considerations, the applied fields should not be very strong, and φ should therefore be small. Given that T_f is constant, this condition allows the

magnetic field B_z to be selected to be small in magnitude. If $\varphi << 1$, the form of (3.7) simplifies, because $A \sim 1$ and $B \sim 0$ (i.e., negligible drag-force), and then,

$\blacktriangledown x = | \eta |(x')$

$\blacktriangledown y = | \eta |(y')$

To summarize: a) From the initial and final positions, the model determines the strength of the magnetic field ($\varphi = | \eta | T_{fn} << 1$) ; b) From the initial and final positions and the expression for the magnetic field, the model predicts the magnitude of the electric field; c) By properly adjusting the fields, an object can be placed at any final location in the xy-plane of the substrate.

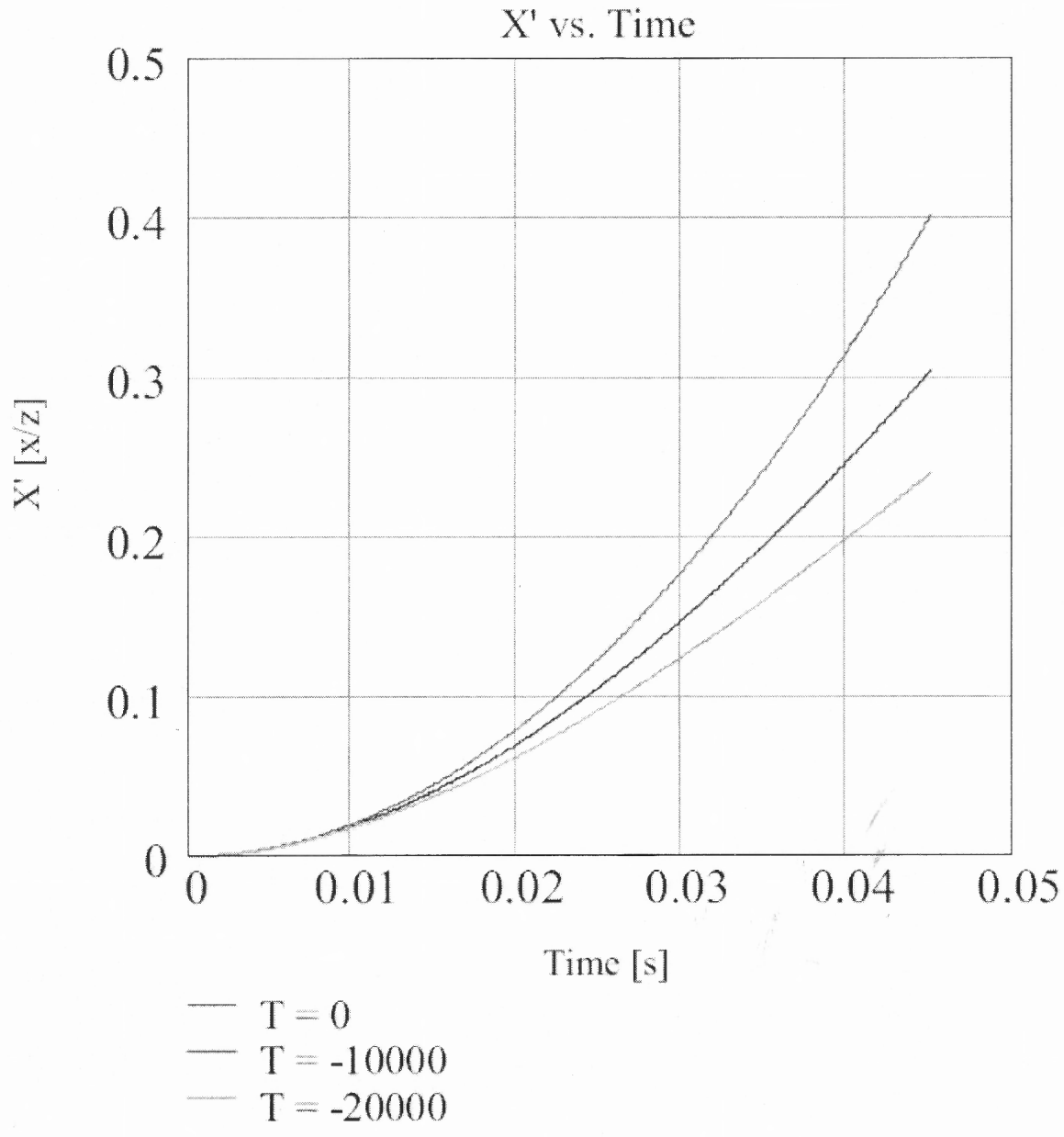

Figure 3.1a The above figure shows the solution for the x and y location of the object versus time for different values of the drag coefficient T. With increasing drag, and all other parameters fixed, the object's motion in the xy-plane is impeded. [23]

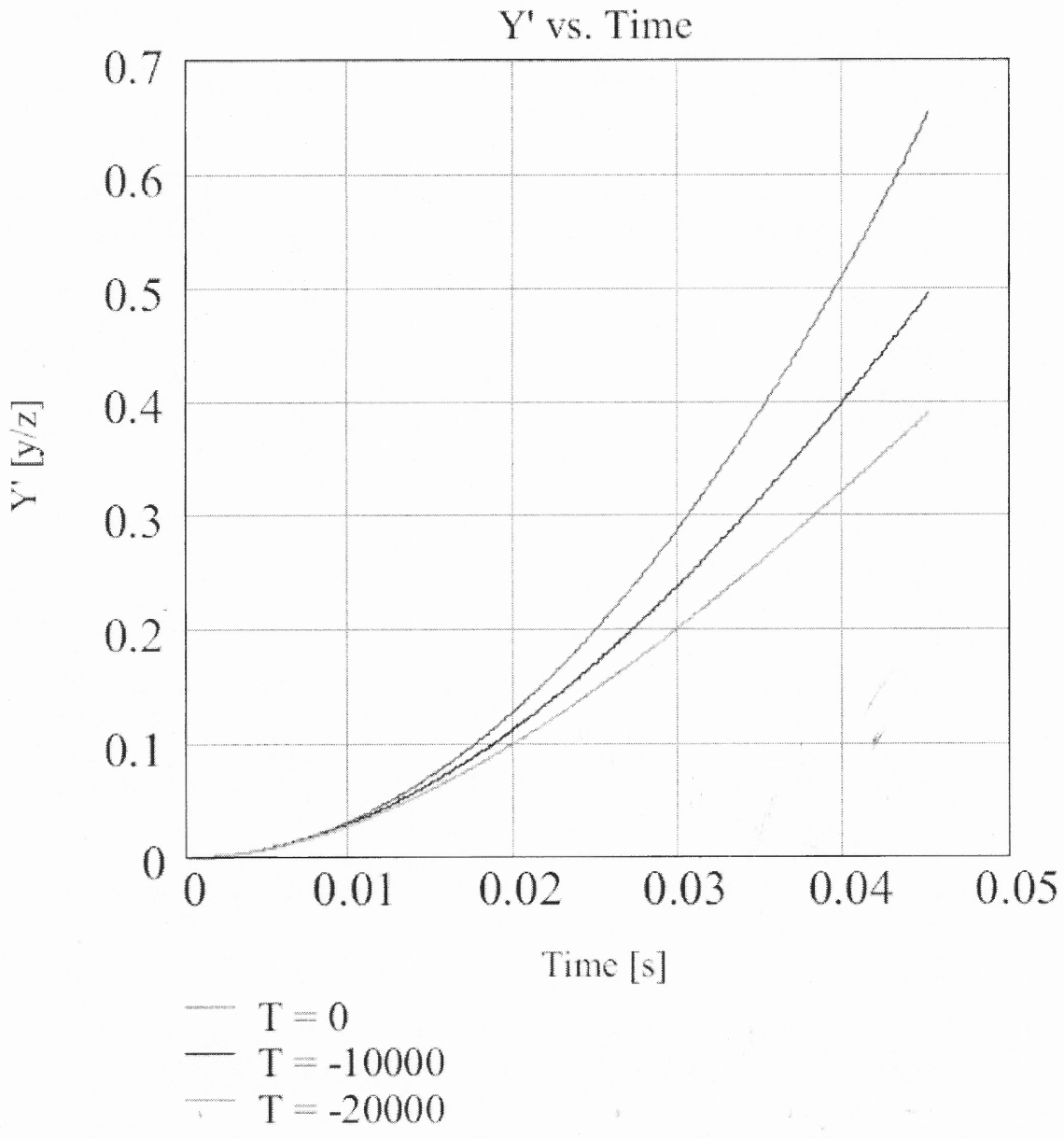

Figure 3.1b The above figure shows the solution for the x and ẏ location of the object versus time for different values of the drag coefficient T. With increasing drag, and all other parameters fixed, the object's motion in the xy-plane is impeded. [23]

For a large drag force, stronger fields are required to bring the object to settle at a desired location. In the Figures (3.1a) and (3.1 b), values of the position parameters are:

initial position = 0, 0, 0.01 (m)

final position = 0.004, 0.0065, 0 (m)

E_x, E_y = 0.1975, 0.3210 (N/C); B_z = 0.1 (mT); e/m = 20 (C/Kg);

g = 9.81 (m/s^2)

For T = 0, $V_{terminal}$ = infinite (no drag force) ($V_{terminal}$ = mg/k)

For T = 10000, $V_{terminal}$ = 0.4905 (m/s)

For T = 20000, $V_{terminal}$ = 0.2453 (m/s) [21]

3.3 Magnetic Field Assisted Assembly

Magnetic field assisted assembly [1] is a technique that is capable of integration of microstructures on to silicon or other semiconductor wafers [1]. This approach is reliable and employs low cost approaches for manufacture. It is shown schematically in Figure 3.2. The approach has two different components - first is the micro components and second is the substrate. The substrate is made from different components, depending on the need, such as, silicon, glass, polymers etc. For optoelectronics device integration, the substrate can be an insulator or a wafer that contains the embedded silicon integrated circuitry.

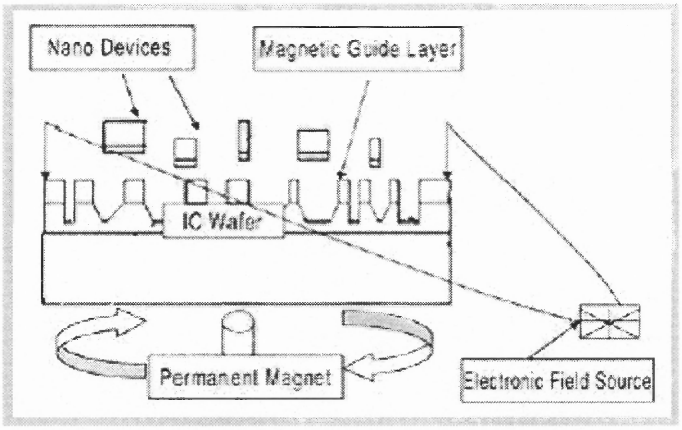

Figure 3.2 A representation of the magnetic field assisted assembly method of integrating micro components and integrated circuits [1]

The recess, shown in Figure 3.2, has to match the dimension of the microelectronic components, so that the components can be placed into desired recesses. The substrate is deposited with ferromagnetic material such as cobalt, nickel or an alloy of cobalt-palladium. This gives the device increased stability and adhesion to the recess on the wafer.

The dimension of microelectronic components plays an important role in device integration. As their sizes decrease, the complexity increases and, thereby, the integration of these devices becomes challenging. The forces at this microscopic level become dominant; for example, the adhesive forces between wafer surface and the object are higher than the gravitational forces. The reasons for these adhesive forces are surface tension, electrostatic forces and Van der waals forces [1] which are difficult to over come.

Electrostatic force of attraction F_{el} *is* due to the Coulomb force between electrically charged objects. The force between the wafer and the device is:

$$F_{el} = \frac{\pi}{4 \cdot \varepsilon_0} \cdot \frac{\varepsilon - \varepsilon_0}{\varepsilon + \varepsilon_0} \cdot d^2 \cdot \sigma^2 \tag{3.8}$$

Where, ε and ε_0 are the dielectric constants of plane and of the air respectively, σ is the surface charge density of the sphere, and d is its diameter. [16]

The Van der Waals force F_{vdw} is an intermolecular force caused by momentary movements of electrons. It is given by the approximate expression,

$$F_{vdw} = \frac{H \cdot d}{12 \cdot z^2} \qquad z \ll d \tag{3.9}$$

for the Van der Waals force between an object (sphere of diameter **d**) and a substrate at distance **z**, where, **H** is the Hamaker constant, the irregularity in the surfaces increase the net distance z and therefore reduce F_{vdw}.

The capillary force F_{cap} is due to a thin liquid film between any two objects, which can originate from the air's humidity. For an object (hydrophilic sphere) with diameter d close to a substrate, the relation can be written as,

$$F_{cap} = \pi \cdot d \cdot \gamma \tag{3.10}$$

The adhesion forces are surface forces and their magnitude is therefore proportional to contact area. Figure 3.3 gives the magnitude of the different types of adhesion force versus distance.

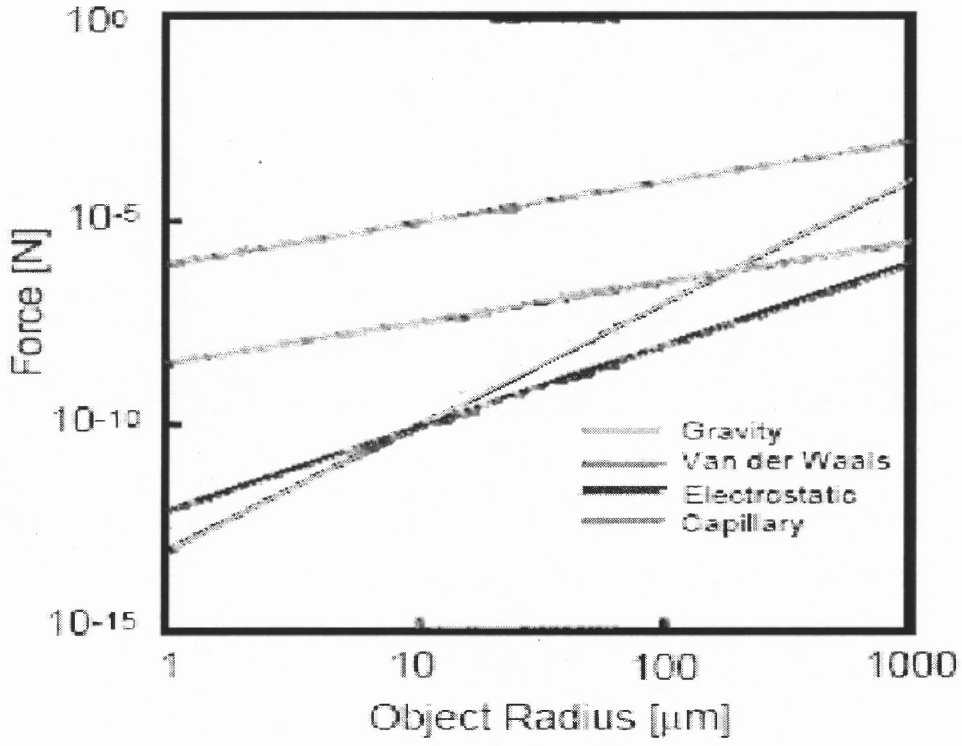

Figure 3.3 The different components of adhesion forces versus distance [1]

There is another way in which the same approach can be used to integrate the devices. This approach uses feed-back tape to assemble the devices. Multiple recesses are made in the wafer that matches with micro components that have to reside on the recess. The micro components are attached temporarily with the feed back tape. After completion of magnetic self-assembly of micro components, individual micro components are attached to the matching recesses on the substrate. The wheels guide the feed back tape, and a magnet moves adjacent and parallel to the substrate. Therefore, the wheels guide the wafer continuously along the chain. The feed tape portion that is parallel to the substrate executes little or no relative motion in the direction parallel to the substrate. The magnet executes either continuous or oscillatory movements in any

direction with respect to the substrate. The micro components that are facing the feedback tape are coated with high permeability ferromagnetic material such as cobalt, nickel or alloy of cobalt-platinum. The coating becomes magnetized when placed in a magnetic field. The magnetic field produced by the moving magnet magnetizes the coating, and the ensuing attractive force pulls the micro components off the tape and into recesses in the substrate. In this alternative method, micro components are pulled preferentially into recesses by several physical characteristics of the magnetic and contact forces [24].

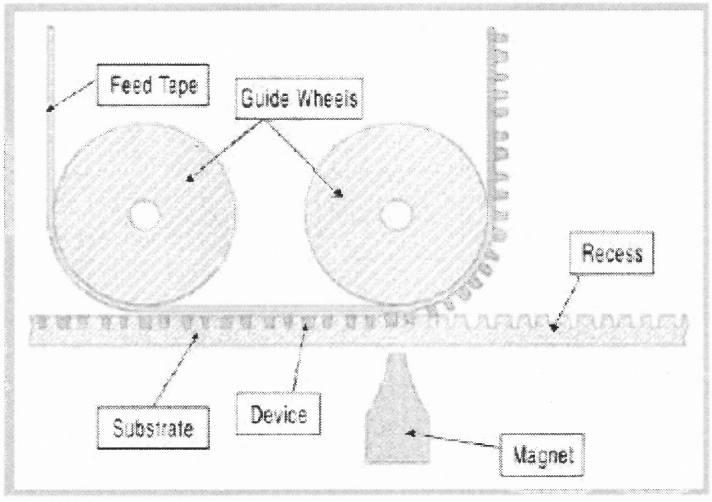

Figure 3.4 A schematic of the magnetic field assisted assembly process using feed tape.

The above method does not depend on statistical randomness [17]. This fact can be analyzed by the behavior of micro components in the magnetic field. Its desirable attribute, when compared to statistical assembly is the scalability to rapid assembly of a plurality of micro components onto a host substrate and the avoidance of frustration effects that lead to assembly errors. Frustration occurs when the path from one or more

micro components to a matching site on the substrate is blocked, or when one or more sites on the substrate remain unoccupied owing to the path being blocked. In addition, magnetic field assisted assembly does not require a liquid carrier medium. It provides a new technique for assembling and integrating micro components onto a silicon wafer or an alternate substrate, and is carried out in such a manner so as to avoid damaging any pre-existing electronics. The process can also take full advantage of very large diameter silicon wafers [23].

3.4 Modeling of Magnetic Field Assisted Assembly

A model [12] that analyzes the force of attraction between the hard magnetic strip and the soft magnetic layer, with air as a medium between them is analyzed in this section. A schematic of the model is shown in the figure below.

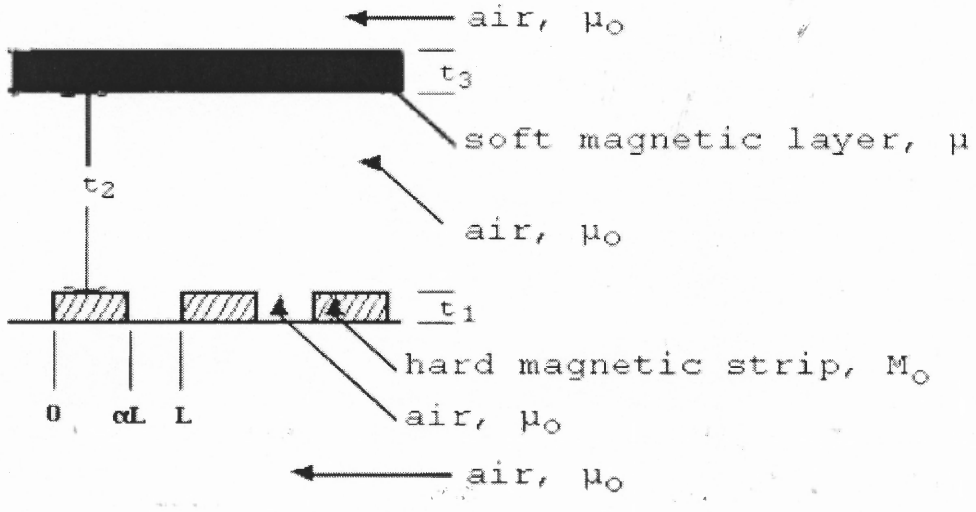

Figure 3.5 A schematic of the model [23].

The soft magnetic layer has a height of t_3, with permeability μ. The height of hard magnetic strip is magnetic t_1, with width αL. The separation between the hard magnetic strips are $(1-\alpha)L$. Here, α is a parameter with $0<\alpha<1$. The vertical separation between soft magnetic layer and hard magnetic strip is of height t_2. There is air between the hard magnetic strips with permeability μ_o.

This model has been originally proposed by Fonstad [12] in the context of MASA. This model is also related to magnetic field assisted assembly (MFAA), and the consideration here is that the magnetized strips and air gaps may have unequal width.

In this model, for assembly, there is no electric field as there is no current source or voltage source; the model has only magnetic forces and it follows Maxwell's laws:

Thus the equations are:

$$\Delta \times \boldsymbol{H}=0 \text{ and } \nabla \cdot \boldsymbol{B}=0. \tag{3.11}$$

The magnetostatic potential φ, is developed across the magnetic regions; so, $\mathbf{H} = -\nabla\varphi$ everywhere. Consider linear, isotropic constitutive relations between the macroscopic magnetic field $\boldsymbol{H}$ and the magnetic induction $\boldsymbol{B}$, so that:

$\boldsymbol{B} = \mu_0 \boldsymbol{H}$ in air

$\boldsymbol{B} = \mu \boldsymbol{H}$ in the soft magnetic layer

$\boldsymbol{B}=\mu_0(\boldsymbol{H}+\boldsymbol{M}_0)$ in the permanent magnetic strips (3.12)

Where, μ_0 and μ are the (constant) permeability of air and the soft magnetic material, respectively, and $\boldsymbol{M}_0$ is the known permanent magnetization of the strips.

So, φ satisfies the Poisson equation, $\nabla^2\varphi = \nabla \cdot \boldsymbol{M}_0$, with source term $\nabla \cdot \boldsymbol{M}_0$. Here, the magnetization $\boldsymbol{M}_0 = M_0 \boldsymbol{j}$ is considered to be constant, where $\boldsymbol{j}$ is a unit vector in the y-

direction normal to the substrate, so that the source term is zero, and the field equation becomes Laplace's equation:

$$\nabla^2 \varphi = 0 \tag{3.13}$$

Boundary conditions at the interface between air and either the soft or permanently magnetized material follow from equations (3.11), which imply that, at an interface, the tangential component of $\boldsymbol{H}$ and the normal component of $\boldsymbol{B}$ are continuous. In terms of the potential φ, using the constitutive relations (3.12), the boundary conditions are that φ is continuous, and, at the interfaces, $y = t_1+t_2$ and $y = t_1+t_2+t_3$, between the soft magnetic material and air:

$$\mu_0 \partial_y \varphi|_A = \mu \partial_y \varphi|_S \tag{3.14}$$

At the vertical sides, $x = 0$, $x = \alpha L$ and $x = (1-\alpha)L$ etc., of the magnetic strips:

$$\partial_x \varphi|_A = \partial_x \varphi|_P \tag{3.15}$$

at the horizontal sides, $0<x<\alpha L$, $y = 0$ and $y = t_1$, of the magnetic strips:

$$\partial_y \varphi|_A - \partial_y \varphi|_P = -M_0 \tag{3.16}$$

The subscripts A, P and S denote evaluation at the air, permanent or soft magnetic side of an interface, respectively. The only forcing or inhomogeneity in the problem for φ appears in this last boundary condition (3.16).

The problem is periodic, with period L in the x-direction, and can be solved by constructing Fourier series in each of the six regions as shown in Figure 3.3, and then applying the continuity and boundary conditions at the interfaces, with the further condition that φ is constant as $y \to \pm\infty$. This leads to a linear algebraic system for the

Fourier coefficients, which can be found in closed form. Details of this part of the analysis are omitted for brevity.

An expression for the force acting on the soft magnetic layer follows by evaluating the integral of the Maxwell stress tensor over the layer's top and bottom surfaces. The general expression for the force $\boldsymbol{f}$ is:

$$\boldsymbol{f}=\mu\int_{\partial\Omega} \boldsymbol{H(H\cdot n)-(1/2)(H\cdot H)n}dS \tag{3.17}$$

where, $\partial\Omega$ is a surface immediately outside the region of interest, $\boldsymbol{n}$ is its outward unit normal and μ is the local permeability. Then, in terms of φ, the force per unit length, $\boldsymbol{F}$, is in the y-direction, i.e. normal to the substrate, and is given by:

$$\boldsymbol{F}=(\mu_0/2)\left(\int_{top} (\partial_y\varphi)^2-(\partial_x\varphi)^2\,dx-\int_{bottom} (\partial_y\varphi)^2-(\partial_x\varphi)^2\,dx\right)\boldsymbol{j} \tag{3.18}$$

where, the integrals over the top and bottom surfaces are evaluated as $y\rightarrow(t_1+t_2+t_3)^+$ and as $y\rightarrow(t_1+t_2)^-$, respectively, with $0<x< L$. A partial check on the expression for the Fourier coefficients is given by noting that the x-component of the force is zero.

When the constructed Fourier series are substituted in (3.18), the expression for the Force per unit length $\boldsymbol{F}$ is:

$$F = -\frac{\mu_0 L}{2}\sum_{n=1}^{\infty}\frac{M_0^2}{\pi^2 n^2}(1-\cos 2n\pi\alpha)e^{-4n\pi t_2/L}\left(1-e^{-2n\pi t_1/L}\right)^2\frac{\sinh\frac{2n\pi t_3}{L}}{\sinh\left(\frac{2n\pi t_3}{L}+\ln\frac{\mu+\mu_0}{\mu-\mu_0}\right)}\,j \tag{3.19}$$

The series converges rapidly as n increases. For α = ½, the strips and air gaps are of equal width, and the series in equation (3.19) is well-approximated by its first term:

$$\boldsymbol{F} = -\frac{\mu_0 L M_0^2}{\pi^2} e^{-4\pi t_2/L}\left(1 - e^{-2\pi t_1/L}\right)^2 \frac{\sinh\frac{2\pi t_3}{L}}{\sinh\left(\frac{2\pi t_3}{L} + \ln\frac{\mu+\mu_0}{\mu-\mu_0}\right)}\ j$$

(3.20)

This is in accord with the expression given by Fonstad [7, 8].

Expressions (3.19) and (3.20) show an exponential decrease of the attractive force acting on the soft magnetic layer with dimensionless distance t_2/L. This is shown in Figure 3.5, which shows a scaled dimensionless force, given by $\boldsymbol{F}$ divided by the n-independent factor on the right-hand side of equation (3.19), versus t_2/L for different values of α with $t_1/L = 0.5$, $t_3/L = 0.1$, and $\mu/\mu_0 = 50$. We find that the force is maximized when the parameter $\alpha = 0.5$ and $t_1/L = 0.5$, i.e., when the permanent magnets and air gaps have equal and square cross-section. Also, from equations (3.19) and (3.20), we see that when μ/μ_0 is large, the attractive force is almost independent of the thickness of the soft magnetic layer t_3/L, unless t_3/L is exceptionally small, like μ_0/μ.

Figure 3.5 shows equipotentials φ = constant, with the same data for $\alpha = 0.5$, $t_1/L = 0.5$, $t_3/L = 0.1$, and $\mu/\mu_0 = 50$ as in Figure 3.4, for two different values of the vertical distance or separation between the permanent magnets and the soft magnetic layer, i.e., $t_2/L = 0.5$ in Figure 3.5(a) and $t_2/L = 0.2$ in Figure 3.5(b). This agrees with the variation of the attractive force with separation distance given in Figure 4. For $t_2/L = 0.5$, the separation is sufficiently large that the potential φ is nearly constant at the soft magnetic layer, so that the magnetic field $\boldsymbol{H}$ and attractive force are relatively weak. However, for decreased

separation $t_2/L = 0.2$, the field at the soft magnetic layer is larger, particularly just below the layer's top and bottom surfaces.

CHAPTER 4

Visualizing Magnetic Fields (VIZIMAG)

ViziMag is a program that has been designed by J. S. Beeteson [25] to give a rapid visualization of magnetic circuit field lines and flux density. ViziMag has been created with the objective of intuitive and rapid model creation, and equally rapid calculation and display of field lines and flux density.

4.1 VIZIMAG - Application to two dimensional fields

ViziMag utilizes methods similar to finite element to evaluate magnetic forces, fields and flux densities by considering point poles and their coordinates in three dimensions. For a permanent magnet, its input parameters are the physical dimensions, permeability and magnetic field strength; one needs to consider the current for solenoids. The output parameters are: flux density, force, force versus distance, field distribution in two dimensions.

ViziMag utilizes the principles of physics and mathematics to map the distribution of magnetic field under various magnetic field sources such as permanent magnets, solenoids, magnets of various shapes and sizes, current carrying conductors, transformers etc. with user defined magnetic strength, permeability etc. The laws of electricity and magnetism in the form of Gauss's law, Ampere's law, Biot-Savart's law, Maxwell's equations and mathematical techniques in the form of Gaussian elimination and related numerical techniques have been employed in ViziMag.

4.2 Gauss' law

Gauss' law [24] explains the relation between the net charges q_{enc} enclosed by the closed

surface and the net flux Φ of an electric field through a closed surface. It is given by:

$$\varepsilon_0 \Phi = \varepsilon_0 \oint \vec{E} \cdot d\vec{A} = q_{enc} \quad (Gauss'law). \tag{4.1}$$

The equation holds only when the net charge is located in a vacuum or in air. The net charge q_{enc} is the algebraic sum of all the enclosed positive and negative charges, and it can be positive, negative, or zero. If q_{enc} is positive, the net flux is outward; if q_{enc} is negative, the flux is inward.

Charge outside the surface, no matter how large or how close it may be, is not included in the term q_{enc} in Gauss' law. The exact form or location of the charges inside the Gauss surface is also of no concern; the only things that matter are the magnitude and sign of the net enclosed charge.

The $\vec{E}$ on the left side, however, is the electric field resulting from all charges, both those inside and those outside the Gaussian surface. [14]

4.3 Biot- Savart law

The magnetic field [26] produced by a short segment of wire ds, carrying current I is:

$$d\mathbf{B} = \frac{\mu_o I}{4\pi} \frac{d\mathbf{s} \times \mathbf{r}}{r^3} \quad , \tag{4.2}$$

Here, the direction of current plays an important role; the current and the parameter $d\mathbf{s}$ is in the same direction which is determined by the direction of current and the vector $\mathbf{r}$ points from the short segment of current to the observation point where we are to compute the magnetic field. In order to find the total current in the circuit, integration

needs to be performed to find the total magnetic field at any point. The constant μ_0 is chosen so that when the current is in amperes and the distances are in meters, the magnetic field is correctly given in units of tesla. Its value in SI units is exactly:

$$\mu_0 = 4\pi \times 10^{-7}\ \mathrm{T \cdot m^2/A} = 1.26 \times 10^{-6}\ \mathrm{T \cdot m/A}\ . \tag{4.3}$$

Infinitely Long Wire: The magnetic field at a point a distance r from an infinitely long wire carrying current I has magnitude:

$$B = \frac{\mu_0 I}{2\pi r} \tag{4.4}$$

and its direction is given by a right-hand rule: point the thumb of your right hand in the direction of the current, and your fingers indicate the direction of the circular magnetic field lines around the wire.

Circular Loop: The magnetic field **at the center** of a circular loop of current-carrying wire of radius R has magnitude:

$$B = \frac{\mu_0 I}{2R} \tag{4.5}$$

and its direction is given by another **right-hand rule**: curl the fingers of your right hand in the direction of the current flow, and your thumb points in the direction of the magnetic field inside the loop.

Long Thick Wire: Imagine a very long wire of radius a carrying current I distributed symmetrically so that the current density, J, is only a function of distance r from the

center of the wire. Ampere's law can be used to find the magnetic field at any radius r outside the wire, where, we have:

$$B = \frac{\mu_o I}{2\pi r} \quad , \tag{4.6}$$

just as if all the current were concentrated at the center of the wire. Inside the wire, where, $r \geq a$

$$B = \frac{\mu_o I(r)}{2\pi r} \quad , \tag{4.7}$$

where, $I(r)$ is the current flowing through the disk of radius r inside the wire; the current outside this disk contributes nothing to the magnetic field at r.

Long Solenoid: For a long solenoid of length L with N turns of wire wrapped evenly along its length, Ampere's law can be used to show that the magnetic field inside the solenoid is uniform throughout the volume of the solenoid (except near the ends where the magnetic field becomes weak) and is given by:

$$B = \mu_o \frac{N}{L} I = \mu_o n I \quad , \tag{4.8}$$

where, $n = N/L$.

Toroid: A toroid consists of N evenly spaced turns of wire carrying current I. (Imagine winding wire onto a bagel, with the wire coming up through the hole, around the outside,

then up through the hole again, etc.). Ampere's law can be used to show that the magnetic field within the volume enclosed by the toroid is given by [27]:

$$B = \frac{\mu_0 NI}{2\pi R}, \tag{4.9}$$

where, R is the distance from the z-axis in cylindrical coordinates, with the z-axis pointing straight up through the hole in the center of the bagel.

4.4 The Maxwell Equations

The Maxwell equations [28, 29] can be written in the following ways:

$$\mathbf{rot}\ \mathbf{H} = \mathbf{j} + \partial\mathbf{D}/\partial t \tag{4.10}$$

$$\mathbf{rot}\ \mathbf{E} = -\partial\mathbf{B}/\partial t \tag{4.11}$$

$$\mathrm{div}\ \mathbf{B} = 0 \tag{4.12}$$

$$\mathrm{div}\ \mathbf{D} = \rho \tag{4.13}$$

Here, **rot** (or **curl** in English literature) is the so called vortex flux density, **H** is the vector of the magnetic field strength, **j** is the current density vector, $\partial\mathbf{D}/\partial t$ is the time derivative of the electric displacement vector **D**, **E** is the electric field strength, $\partial\mathbf{B}/\partial t$ is the time derivative of the magnetic induction vector **B**, div is the so called source density and ρ is the charge density.

The global or integral forms of the Maxwell equations are written in terms of path, surface, and volume integrals and are:

$$\oint_C \mathbf{H}\cdot\mathbf{dr} = I + I^{DISP} \tag{4.14}$$

$$\oint_C \mathbf{E}\cdot\mathbf{dr} = \partial\Phi_B/\partial t \tag{4.15}$$

$$\oint_A \mathbf{B}\cdot\mathbf{dA} = 0 \tag{4.16}$$

$$\oint_A \mathbf{D}\cdot\mathbf{dA} = \int_V \rho dV \tag{4.17}$$

where,

I is the electric current $I = \int_A \underline{\mathbf{j}}\cdot\mathbf{dA}$,

I^{DISP} is the so called displacement $I^{DISP} = \int_A (\partial\mathbf{D}/\partial t)\cdot\mathbf{dA}$, and

Φ_B is the flux of the magnetic induction **B**, $\Phi_B = \int_A \mathbf{B}\cdot\mathbf{dA}$.

The two variables that describe the electrical properties of the electromagnetic fields are **E** and **D**, and also two variables for the magnetic properties of the field are **H** and **B**. This is necessary when some materials are present with oriented electric and magnetic dipoles. If the electric dipole density is denoted by **P** and the magnetic dipole density by **M**, then we can use the following definitions for **D** and **B**:

$$\mathbf{D} = \varepsilon_0\mathbf{E} + \mathbf{P} \quad \text{and,} \tag{4.18}$$

$$\mathbf{B} = \mu_0\mathbf{H} + \mathbf{M} \tag{4.19}$$

Here, ε_0 and μ_0 are the permittivity and the permeability of the vacuum, respectively. For vacuum (**P** = 0, **M** =0), the Maxwell equations can be written in the following form:

$$\mathbf{rot\ H} = \underline{\mathbf{j}} + \varepsilon_0\partial\mathbf{E}/\partial t \tag{4.20}$$

$$\mathbf{rotE} = -\mu_0\partial\mathbf{H}/\partial t \tag{4.21}$$

$$\text{div } \mathbf{H} = 0 \tag{4.22}$$

$$\text{div } \mathbf{E} = \rho/\varepsilon_0 \tag{4.23}$$

Thus, we can see that, in this case, there is only one variable for the electric field **E**, and another variable **H** for the magnetic field. In other words, the introduction of two more variables, **D** and **B** (or **P** and **M**), is necessary if we have not only vacuum, but also some other medium. In order to determine $\underline{\mathbf{j}}$, **P**, and **M** for a certain material in the medium, we use the so called material equations:

$$\underline{\mathbf{j}} = \underline{\mathbf{j}}(\mathbf{E}, \mathbf{E}^i),\ \mathbf{P} = \mathbf{P}(\mathbf{E}),\ \text{and}\ \mathbf{M} = \mathbf{M}(\mathbf{H}) \tag{4.24}$$

Here, $\mathbf{E}^i$ includes all non electromagnetic forces. The various functions in the material equations can be different for each material, but they are often linear. In this case, the material equations are written in the following form:

$$\underline{\mathbf{j}} = \sigma\cdot(\mathbf{E} + \mathbf{E}^i),\quad \mathbf{P} = \chi_e\cdot\varepsilon_0\cdot(\mathbf{E}),\ \text{and}\ \mathbf{M} = \chi_m\cdot\mu_0\cdot(\mathbf{H}), \tag{4.25}$$

where, σ is the electric conductivity, χ_e is the electric and χ_m is the magnetic susceptibility.

Thus, the governing equations of electromagnetism include the four Maxwell equations and the three material equations. Finally, one more equation is needed to establish a connection with mechanics; for example,

$$\mathbf{f} = \rho\cdot\mathbf{E} + \mathbf{j}\times\mathbf{B} \tag{4.26}$$

where, **f** is the mechanical force density (force acting on the unit volume). Another possibility to establish the connection to mechanic is:

$$\rho_{EE} = \tfrac{1}{2}(\mathbf{E}\cdot\mathbf{D} + \mathbf{H}\cdot\mathbf{B}) \tag{4.27}$$

where, ρ_{EE} is the electromagnetic energy density, that is the energy stored by the electric and magnetic fields in unit volume. (The concept of force and energy were developed already in mechanics.) [32]

4.5 Axial Field of a Finite Solenoid

This formula [33] uses the equation for the field due to a thin shell solenoid, integrated over a range of radii to obtain the magnetic field at any point on the axis of a finite solenoid [33].

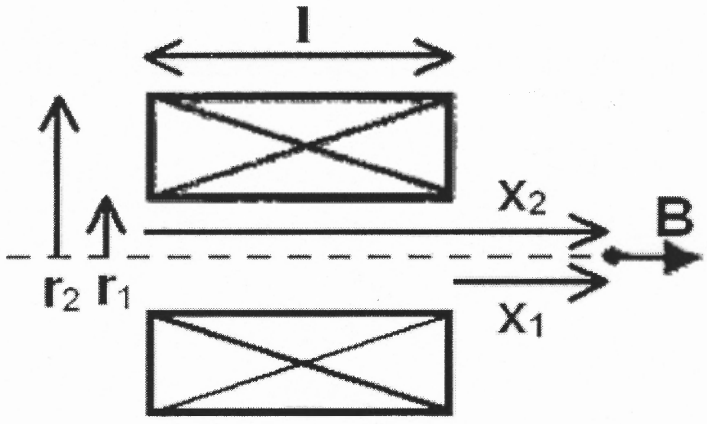

Figure 4.1 Solenoid in cross section view [33].

$$B = \frac{\mu_o in}{2(r_2 - r_1)}\left[x_2 \ln \frac{\sqrt{r_2^2 + x_2^2} + r_2}{\sqrt{r_1^2 + x_2^2} + r_1} - x_1 \ln \frac{\sqrt{r_2^2 + x_1^2} + r_2}{\sqrt{r_1^2 + x_1^2} + r_1}\right] \tag{4.28}$$

General Case:

B is the magnetic field, in teslas, at any point on the axis of the solenoid. The direction of the field is parallel to the solenoid axis.

Here, μ_o is the permeability constant, i is the current in the wire, in amperes, **n** is the number of turns of wire per unit length in the solenoid, $\mathbf{r_1}$ is the inside radius of the solenoid, $\mathbf{r_2}$ is the outside radius of the solenoid, $\mathbf{x_1}$ and $\mathbf{x_2}$ are the distances, on axis, from the ends of the solenoid to the magnetic field measurement point.

$$B = \mu_o \sqrt{\frac{P\lambda}{r_1 \rho}} G \tag{4.29}$$

where, **G** is the unit less geometry factor:

$$G = \sqrt{\frac{1}{8\pi\beta(\alpha^2 - 1)}} \left[(\gamma + \beta) \ln \frac{\alpha + \sqrt{\alpha^2 + (\gamma + \beta)^2}}{1 + \sqrt{1 + (\gamma + \beta)^2}} - (\gamma - \beta) \ln \frac{\alpha + \sqrt{\alpha^2 + (\gamma - \beta)^2}}{1 + \sqrt{1 + (\gamma - \beta)^2}} \right] \tag{4.30}$$

$$\alpha = \frac{r_2}{r_1} \quad \beta = \frac{l}{2r_1} \quad \gamma = \frac{x_1 + x_2}{2r_1} \tag{4.31}$$

Special Case: $x_1=(-x_2)$ The magnetic field measurement point is at the center of the solenoid.

$$B = \frac{\mu_o i N}{2(r_2 - r_1)} \ln \frac{\sqrt{r_2^2 + (l/2)^2} + r_2}{\sqrt{r_1^2 + (l/2)^2} + r_1} \tag{4.32}$$

...or

$$B = \frac{\mu_o j l}{2} \ln \frac{\sqrt{r_2^2 + (l/2)^2} + r_2}{\sqrt{r_1^2 + (l/2)^2} + r_1} \tag{4.33}$$

j is the current density in the coil cross section, in amps/(unit area).

l is the length of the coil.

N is the total number of turns of wire in the coil.

and the unit less geometry factor G is simply:

$$G = \sqrt{\frac{\beta}{2\pi(\alpha^2 - 1)}} \ln \frac{\alpha + \sqrt{\alpha^2 + \beta^2}}{1 + \sqrt{1 + \beta^2}} \tag{4.34}$$

4.6 Mathematical Techniques

Gaussian elimination:

This technique employs solving linear system of n equations with n unknowns x_1, x_2, $x_3 \ldots x_n$:

$$\begin{cases} a_{12}x_1 + a_{12}x_2 + \ldots + a_{1n}x_n = b_1 \\ a_{21}x_1 + a_{22}x_2 + \ldots + a_{2n}x_n = b_2 \\ \qquad\qquad \vdots \\ a_{n1}x_1 + a_{n2}x_2 + \ldots + a_{nn}x_n = b_n \end{cases} \tag{4.35}$$

In the matrix form, we have

$$Ax = \begin{pmatrix} a_{11} & a_{12} & \cdots & a_{1n} \\ a_{21} & a_{22} & \cdots & a_{2n} \\ \vdots & \vdots & \ddots & \vdots \\ a_{n1} & a_{n2} & \cdots & a_{nn} \end{pmatrix} \begin{pmatrix} x_1 \\ x_2 \\ \vdots \\ x_n \end{pmatrix} = \begin{pmatrix} b_1 \\ b_2 \\ \vdots \\ b_n \end{pmatrix} = b \tag{4.36}$$

4.6.1 Gaussian Elimination Algorithm: Forward Elimination and Triangular Form

$$k = 1, \ldots, n-1 \begin{cases} a_{ij}^{(k+1)} = a_{ij}^{(k)} & i = 1, \ldots, k \quad j = 1, \ldots, n \\ a_{ij}^{(k+1)} = 0 & i = k+1, \ldots, n \quad j = 1, \ldots, k \\ a_{ij}^{(k+1)} = a_{ij}^{(k)} - \dfrac{a_{ik}^{(k)} a_{kj}^{(k)}}{a_{kk}^{(k)}} & i = k+1, \ldots, n \quad j = k+1, \ldots, n \\ b_i^{(k+1)} = b_i^{(k)} & i = 1, \ldots, k \\ b_i^{(k+1)} = b_i^{(k)} - \dfrac{a_{ik}^{(k)} b_k^{(k)}}{a_{kk}^{(k)}} & i = k+1, \ldots, n \end{cases} \tag{4.37}$$

Let U be the triangular upper matrix; we have,

$$U = (u_{ij})_{1 \le i,j \le n} = (a_{ij}^{(n)})_{1 \le i,j \le n} \tag{4.38}$$

4.6.2 Gaussian Elimination Algorithm: Backward Elimination

Now, the matrix A is in triangular form U; we can solve:

$$Ux = b^{(n)} \tag{4.39}$$

with b(n) as the second member after the same operations as U.

We use a backward elimination for solving U(x) =b (n) [8]:

$$\begin{cases} x_n = \dfrac{y_n}{u_{nn}} = \dfrac{y_n}{a_{nn}^{(n)}}; \\ x_i = \dfrac{1}{u_{ii}}\left(y_i - \sum_{j=i+1}^{n} u_{ij}x_j\right) = \dfrac{1}{a_{ii}^{(n)}}\left(y_i - \sum_{j=i+1}^{n} a_{ij}^{(n)}x_j\right) \quad \forall i = n-1, n-2, \ldots, 1. \end{cases} \tag{4.40}$$

Equations Solved Numerically

One of the most popular techniques for solving simultaneous linear equations is the Gaussian elimination method. The approach is designed to solve a general set of *n* equations and *n* unknowns:

$$a_{11}x_1 + a_{12}x_2 + a_{13}x_3 + \ldots + a_{1n}x_n = b_1$$

$$a_{21}x_1 + a_{22}x_2 + a_{23}x_3 + \ldots + a_{2n}x_n = b_2$$

. .

$$a_{n1}x_1 + a_{n2}x_2 + a_{n3}x_3 + \ldots + a_{nn}x_n = b_n \tag{4.41}$$

Gaussian elimination consists of two steps:

1. Forward Elimination of Unknowns: In this step, the unknown is eliminated in each equation starting with the first equation. This way, the equations are "reduced" to one equation and to one unknown in each equation.

2. Back Substitution In this step, starting from the last equation, each of the unknowns is found.

Forward Elimination of Unknowns:

In the first step of forward elimination, the first unknown, x_1 is eliminated from all rows below the first row. The first equation is selected as the pivot equation to eliminate x_1. Thus, to eliminate x_1 in the second equation, one divides the first equation by a_{11} (hence called the pivot element) and it is then multiplied by a_{21}. This is the same as multiplying the first equation by a_{21}/ a_{11}. This gives:

$$a_{21}x_1 + \frac{a_{21}}{a_{11}}a_{12}x_2 + \ldots + \frac{a_{21}}{a_{11}}a_{1n}x_n = \frac{a_{21}}{a_{11}}b_1 \tag{4.42}$$

Now, this equation can be subtracted from the second equation to yield:

$$\left(a_{22} - \frac{a_{21}}{a_{11}}a_{12}\right)x_2 + \ldots + \left(a_{2n} - \frac{a_{21}}{a_{11}}a_{1n}\right)x_n = b_2 - \frac{a_{21}}{a_{11}}b_1 \tag{4.43}$$

Or

$$a_{22}^{'}x_2 + ... + a_{2n}^{'}x_n = b_2^{'} \tag{4.44}$$

where,

$$a_{22}^{'} = a_{22} - \frac{a_{21}}{a_{11}}a_{12}$$

$$\vdots$$

$$a_{2n}^{'} = a_{2n} - \frac{a_{21}}{a_{11}}a_{1n}$$

This procedure of eliminating x_1 is now repeated for the third equation to the nth equation to reduce the set of equations to:

$$a_{11}x_1 + a_{12}x_2 + a_{13}x_3 + ... + a_{1n}x_n = b_1$$

$$a_{22}^{'}x_2 + a_{23}^{'}x_3 + ... + a_{2n}^{'}x_n = b_2^{'}$$

$$a_{32}^{'}x_2 + a_{33}^{'}x_3 + ... + a_{3n}^{'}x_n = b_3^{'}$$

. . .

. . .

. . .

$$a_{n2}^{'}x_2 + a_{n3}^{'}x_3 + ... + a_{nn}^{'}x_n = b_n^{'} \tag{4.45}$$

This is the end of the first step of forward elimination. Now, for the second step of forward elimination, we start with the second equation as the pivot equation and a'_{22} as the pivot element. Therefore, to eliminate x_2 in the third equation, one divides the second equation by a'_{22} (the pivot element) and it is then multiplied by a'_{32}, that is, the same as multiplying the second equation by a'_{32}/a'_{22} and subtracting from the third equation.

This makes the coefficient of x_2 to be zero in the third equation. The same procedure is now repeated for the fourth equation till the nth equation to yield:

$$a_{11}x_1 + a_{12}x_2 + a_{13}x_3 + \ldots + a_{1n}x_n = b_1$$

$$a'_{22}x_2 + a'_{23}x_3 + \ldots + a'_{2n}x_n = b'_2$$

$$a''_{33}x_3 + \ldots + a''_{3n}x_n = b''_3$$

. .

. .

. .

$$a''_{n3}x_3 + \ldots + a''_{nn}x_n = b''_n \qquad (4.46)$$

The next subsequent steps of forward elimination are performed by using the third equation as a pivot equation and so on. That is, there will be a total of (n-1) steps of forward elimination. At the end of (n-1) steps of forward elimination, we get a set of equations that look like:

$$a_{11}x_1 + a_{12}x_2 + a_{13}x_3 + \ldots + a_{1n}x_n = b_1$$

$$a'_{22}x_2 + a'_{23}x_3 + \ldots + a'_{2n}x_n = b'_2$$

$$a''_{33}x_3 + \ldots + a''_{n}x_n = b''_3$$

. .

. .

. .

$$a_{nn}^{(n-1)} x_n = b_n^{(n-1)} \tag{4.47}$$

Back Substitution:

Now, the equations are solved starting from the last equation as it has only one unknown.

$$x_n = \frac{b_n^{(n-1)}}{a_{nn}^{(n-1)}} \tag{4.48}$$

Then, the second last equation, that is the $(n\text{-}1)^{th}$ equation, has two unknowns - x_n and x_{n-1}, but x_n is already known. This reduces the $(n\text{-}1)^{th}$ equation also to one unknown. Hence, back substitution can be represented for all equations by the formula [31]:

$$x_i = \frac{b_i^{(i-1)} - \sum_{j=i+1}^{n} a_{ij}^{(i-1)} x_j}{a_{ii}^{(i-1)}} \quad \text{for } i=n-1, n-2, \ldots, 1 \tag{4.49}$$

and

$$x_n = \frac{b_n^{(n-1)}}{a_{nn}^{(n-1)}} \tag{4.50}$$

CHAPTER 5

VIZIMAG SIMULATIONS

In this chapter, the simulations of the magnetic field distributions and the forces experienced by the devices, as a function a number of parameters including distance between the two electromagnets in the form of solenoids, position of the device, permeability of the magnetic layer in the recess and at the bottom of the device and the core of the solenoid, is presented.

The proposed approach for the simulations is the following: A wafer of width 110 mm containing a chosen number of recesses of desired width and desired spacing between recesses is considered. In order to assist with the magnetic field assisted assembly process, two programmable solenoids with desired dimensions and desired permeability of the cores of the solenoids are considered and are located below the wafer. The solenoids chosen for this simulation are 10mm in width and 50 mm in length. For simplicity, the presence of only one device, on the wafer, that needs to be placed in the desired recess, is considered. With the solenoids initially located at the extreme ends of the wafer, the spacing between the solenoids is 90mm. The recesses contain hard magnetic material; the bottom of the devices is coated with soft magnetic material.

Four case studies that consider the location of the recesses relative to the device for optimal placement of the device in the recess have been investigated here. The criteria for the choice of the four case studies have been determined by the width of the recesses and the spacing between the recesses (medium) and the directionality of movement of the magnetic field source.

Two programmable solenoids have been considered as sources of magnetic field and are placed below and adjacent to the wafer. The programmable parameters of the solenoids include the current, the number of turns, length and width of the solenoid, diameter of the solenoid and the permeability of the core material inside the solenoid. The details of the various parameters, utilized in the simulation are summarized in Figure 5.1a and Tables 5.1 – 5.4.

The details of the case studies, considered in the various simulations are as follows:

5.1 Case I

Case I – When the dimensions of air (spacing between the devices) and the width of the hard magnetic material within the recess are different and the external magnetic field sources (two solenoids) are moving towards each other in such a way that the distance between the two solenoids is reduced in steps of 10mm.

The results of the simulation of the magnetic field, in Figure 5.1 (b), represent the situation of Case 1 when the distance between the solenoids is reduced by 10mm. The simulations show magnetic field lines and the force experienced by the device.

The software, ViziMag [32], has built-in capabilities for designing different magnetic and non- magnetic materials of desired shapes and sizes.

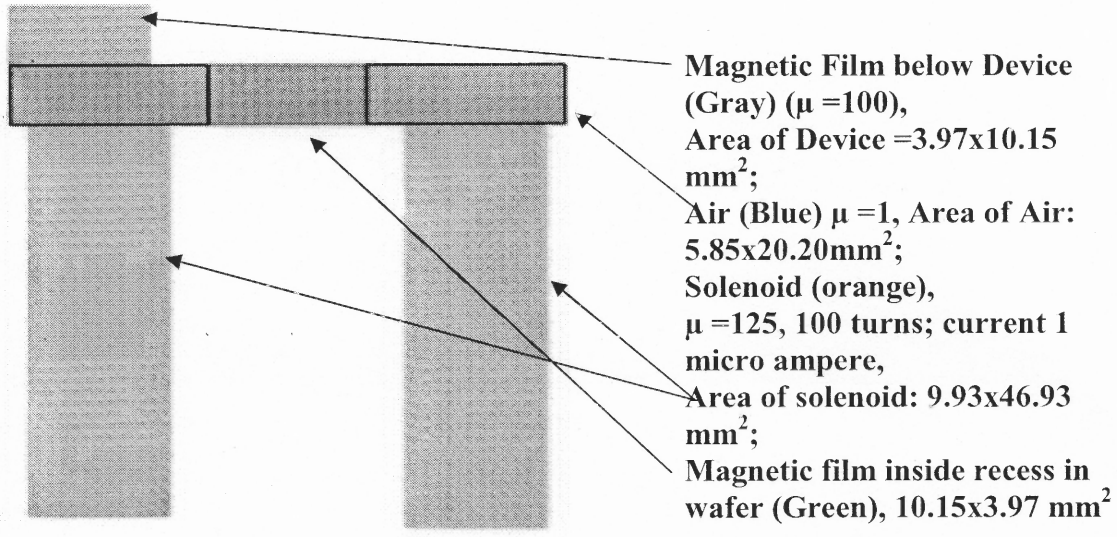

Figure 5.1a Schematic of the conceptual approach for modeling of magnetic field assisted assembly.

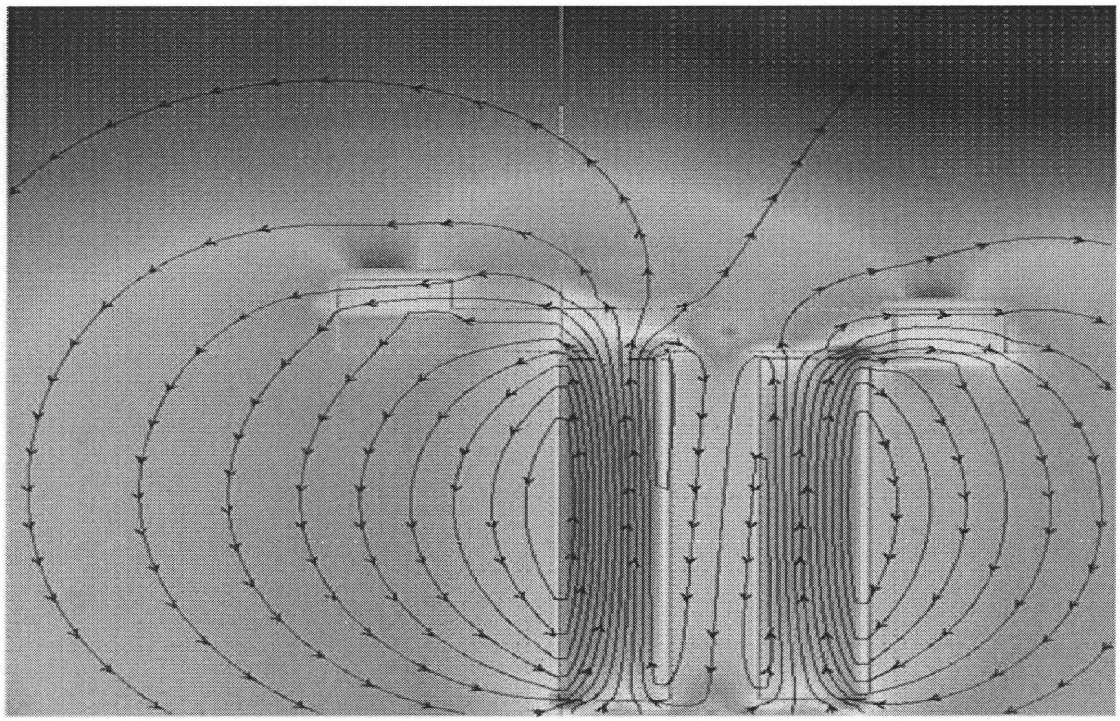

Figure 5.1b A simulation in which dimension of air and metal are different and external field source is moving; Case I; $B_x = -1.5 \times 10^{-10}$T; $B_y = -1.4 \times 10^{-11}$T; $B = 4.3 \times 10^{-10}$T.

In Figure 5.1 (c), the results of a simulation, in which the dimension of air (spacing between recesses) and metal (hard magnetic material deposited in the bottom of the recess – i.e., the width of the recess) are different and the solenoids are moving towards each other, are presented. The distance between the solenoids is reduced by 30mm from their initial positions.

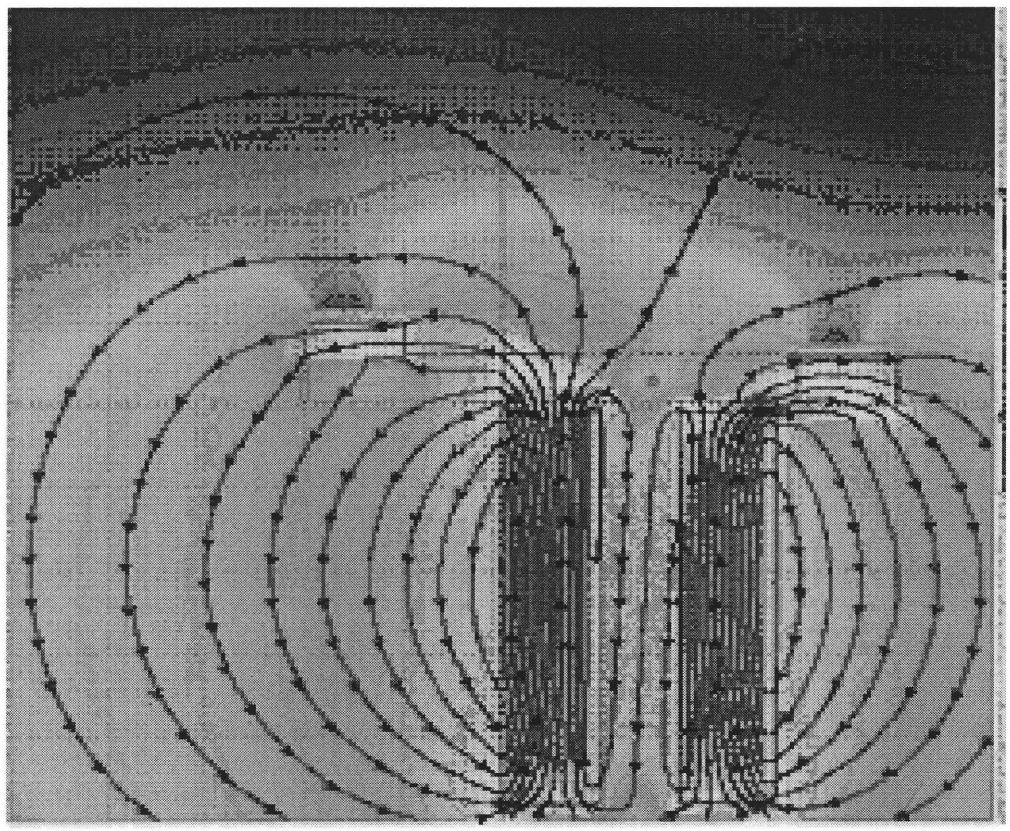

Figure 5.1c A simulation in which dimension of air and metal are different and external field source is moving; Case I; B_x = - 4.24x10 $^{-10}$T; B_y = 7.25x10 $^{-11}$T; B = 4.3x10 $^{-10}$T.

In Table 5.1, the details of the physical dimensions, permeability of the materials and the magnetic strength of the solenoids are summarized. The distance between the solenoids, in their initial positions, is 90 grid units (90mm).

Mesh size	1 mm
Dimension Soft magnetic material below the device	10.15 mm by 3.97 mm
Permeability of the soft magnetic material	125
Dimension of the air between the magnetic material	5.85 mm by 20.20 mm
Permeability of air	1
Dimension of Hard magnetic material in the substrate	5.96 mm by 10.04 mm
Permeability of the hard magnetic material (between airs)	125
Dimensions of the magnet	10 mm by 50 mm
Permeability of the magnet	125
Number of turns	100
Current in solenoid	1 μamp
Number of magnets	2

Table 5.1: Physical parameters considered when the solenoids are moved towards each other; the width of magnetic layer (on the substrate) and the width of the air between the magnetic materials (spacing between the recesses) is different.

5.2 Case II

Case II – When the dimensions of air (spacing between the devices) and the width of the hard magnetic material within the recess are different and the device is moved by 5 mm from its initial position towards the right (i.e., towards the solenoid on the right).

The results of this simulation are presented in Figure 5.2 (a). From these simulations, the magnetic fields and the force experienced by the device can be calculated.

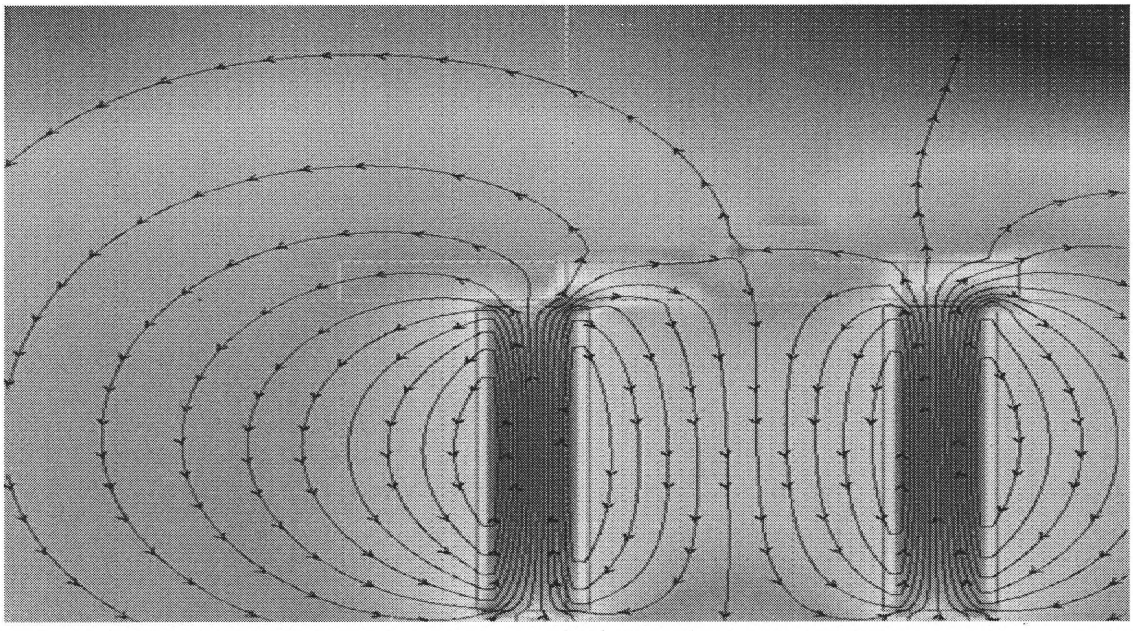

Figure 5.2a A simulation in which dimension of air and metal are different and device is moving; Case II; $B_x = 1.77 \times 10^{-9}$T; $B_y = 9.67 \times 10^{-10}$T; $B = 2.02 \times 10^{-9}$T.

In Figure 5.2 (b), the results of magnetic field lines and force, in which the dimension of air (spacing between recesses) and metal (hard magnetic material deposited in the bottom of the recess – width of the recess) are different and the device is moving towards the right solenoid by 45mm, are presented.

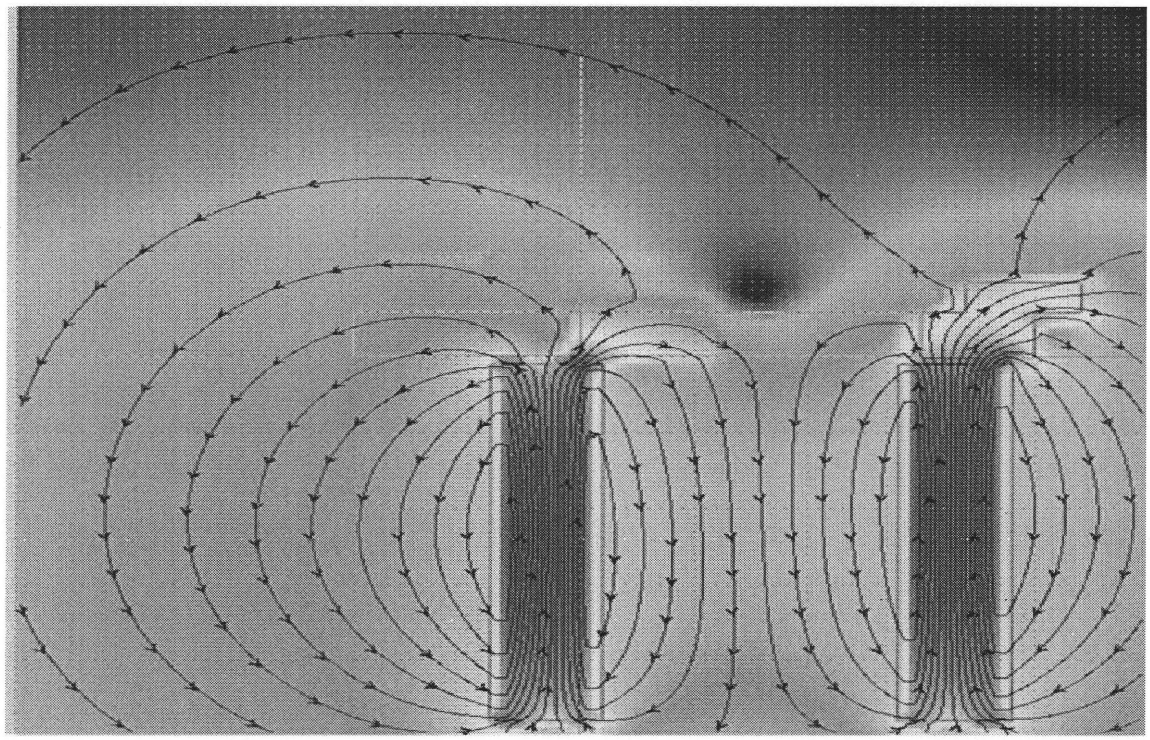

Figure 5.2b A simulation in which dimension of air and metal are different and device is moving; Case II; $B_x = -3.62 \times 10^{-10}$T; $B_y = 1.65 \times 10^{-11}$T; $B = 3.62 \times 10^{-10}$T.

In Table 5.2, the details of the physical dimensions, permeability of the materials and the magnetic strength of the solenoids are presented. The distance between the solenoids is 90 grid units.

Mesh size	1 mm
Dimension Soft magnetic material below the device	10.15 mm by 3.97 mm
Permeability of the soft magnetic material	125
Dimension of the air between the magnetic material	5.85 mm by 20.20 mm
Permeability of air	1
Dimension of Hard magnetic material in the substrate	5.85 mm by 20.20 mm
Permeability of the hard magnetic material (between airs)	125
Dimensions of the magnet	10 mm by 50 mm
Permeability of the magnet	125
Number of turns	100
Current in solenoid	1 μamp
Number of magnets	2

Table 5.2: Physical parameters considered when the device is moved on the substrate towards the right; the width of the magnetic layer (in the recess on the substrate) and the width of the air between the magnetic material is different. (Case 2)

5.3 Case III

Case III – When the dimensions of air (spacing between the devices) and the width of the hard magnetic material within the recess are same and the device is moving towards the right by 40 mm from its initial position (i.e., towards the solenoid on the right).

In Figure 5.3 (a), the results of magnetic field lines and force, in which the dimension of air (spacing between recesses) and metal (hard magnetic material deposited in the bottom of the recess – width of the recess) are same and the device is moving towards the right solenoid by 40mm from its initial position, are presented.

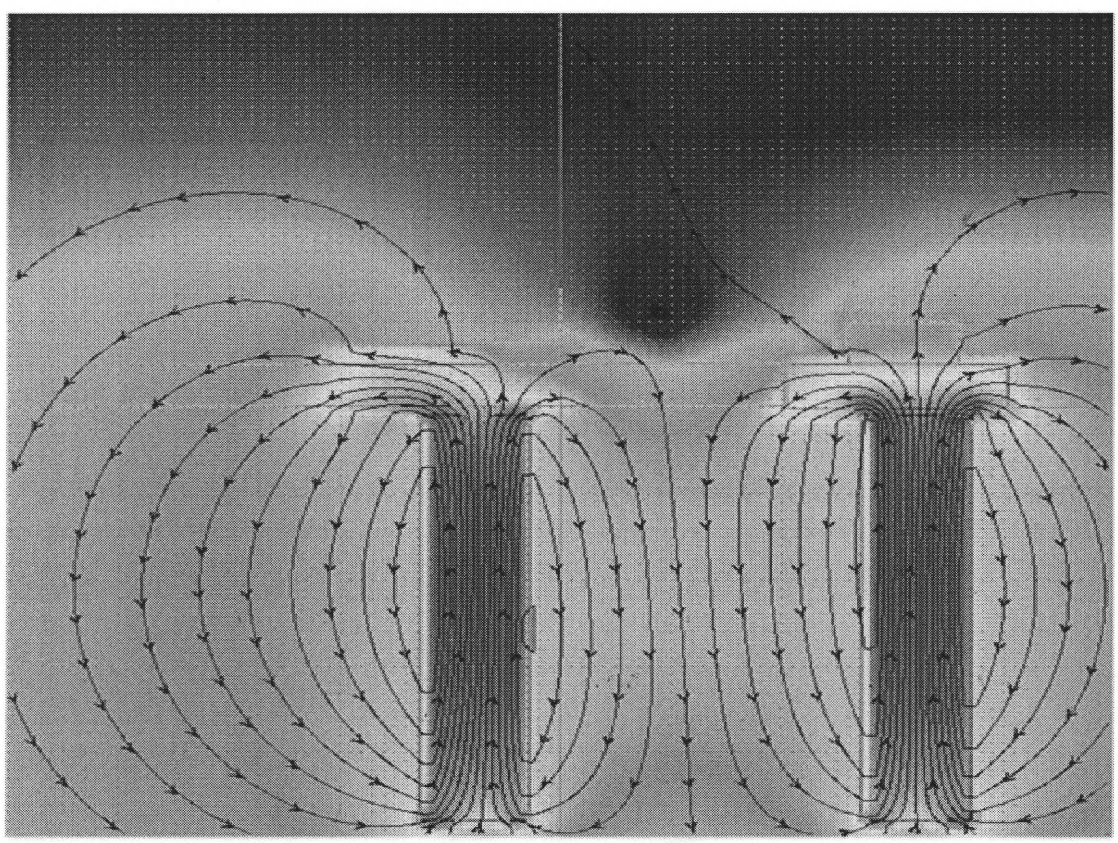

Figure 5.3a A simulation in which dimensions of air and metal are same and device is moving; Case III; $B_x = 1.33 \times 10^{-9}$T; $B_y = -5.41 \times 10^{-10}$T; $B = 1.43 \times 10^{-9}$T.

The results in Figure 5.3 (b) represent the situation of case 3 with the device moving towards the right by 25 mm from its initial position.

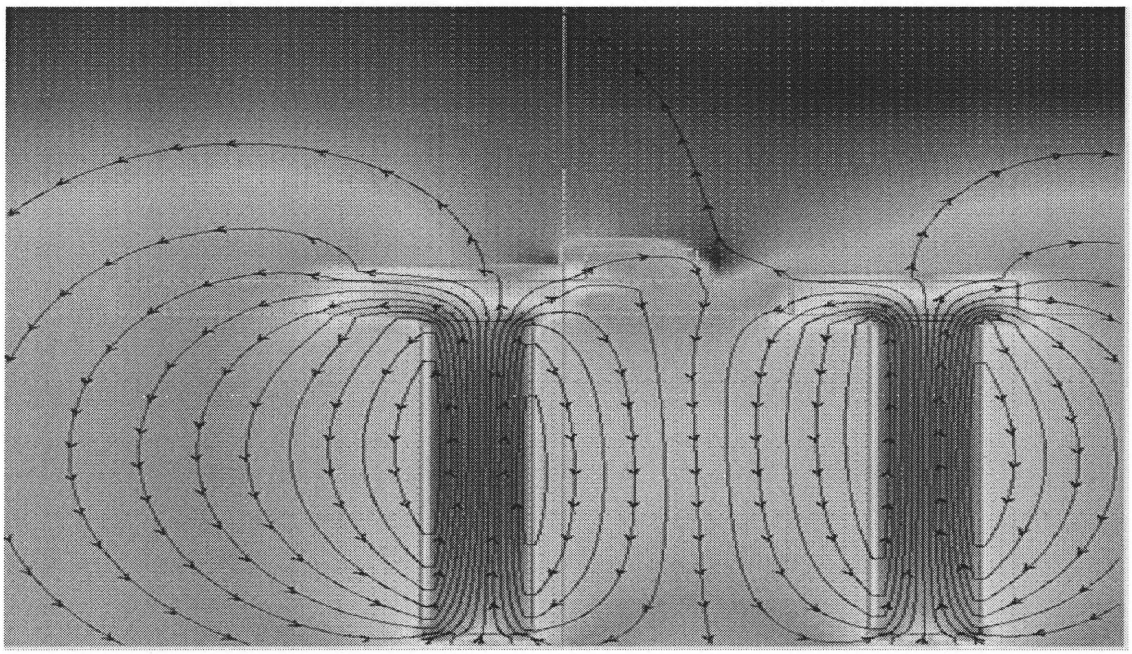

Figure 5.3b A simulation in which dimensions of air and metal are same and device is moving; Case III; $B_x = 7.52 \times 10^{-10} T$; $B_y = 4.82 \times 10^{-9} T$; $B = 4.88 \times 10^{-9} T$.

In Table 5.3, the details of the physical dimensions, permeability of the materials and the magnetic strength of the solenoids are presented. The distance between the solenoids is 90 grid units.

Mesh size	1 mm
Dimension Soft magnetic material below the device	9.93 mm by 4.75 mm
Permeability of the soft magnetic material	125
Dimension of the air between the magnetic material	4.97 mm by 20.20 mm
Permeability of air	1
Dimension of Hard magnetic material in the substrate	4.9 mm by 20.20 mm
Permeability of the hard magnetic material (between airs)	125
Dimensions of the magnet	10 mm by 50 mm
Permeability of the magnet	125
Number of turns	100
Current in solenoid	1 μamp
Number of magnets	2

Table 5.3: Physical parameters considered when the device is moved towards the right; the width of the magnetic layer (on the substrate) and the width of the air (spacing) between the recesses is same. (Case III)

5.4 Case IV

Case IV – When the dimensions of air (spacing between the devices) and the width of the hard magnetic material within the recess are same and the field sources are moving towards each other; the distance between the solenoids is reduced by 10mm from their initial positions.

In Figure 5.4(a), the results of the simulation of magnetic fields and the force experienced by the device (of case 4) are presented.

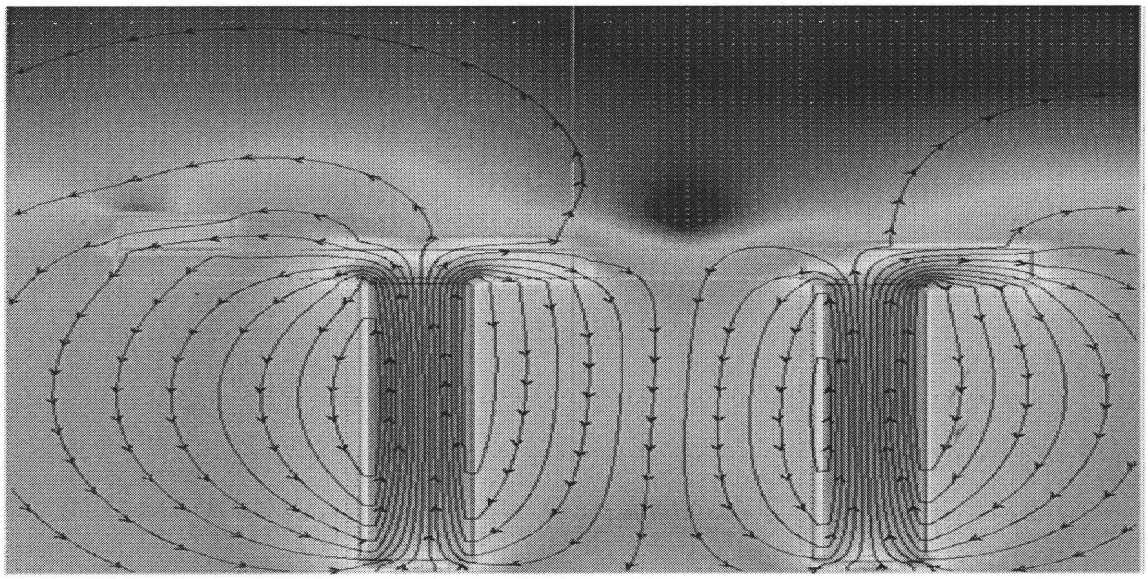

Figure 5.4a) A simulation in which dimensions of air and metal are same and external field sources are moved towards each other from their initial positions; Case IV; B_x = 8.62×10^{-9}T; $B_y = 1.65 \times 10^{-10}$T; $B = 8.62 \times 10^{-9}$T.

In Figure 5.4 (b), a simulation of magnetic fields and forces experienced by the device, in which the dimension of air (spacing between recesses) and metal (hard magnetic material deposited in the bottom of the recess – width of the recess) are same and the solenoids are moving towards each other, are presented.

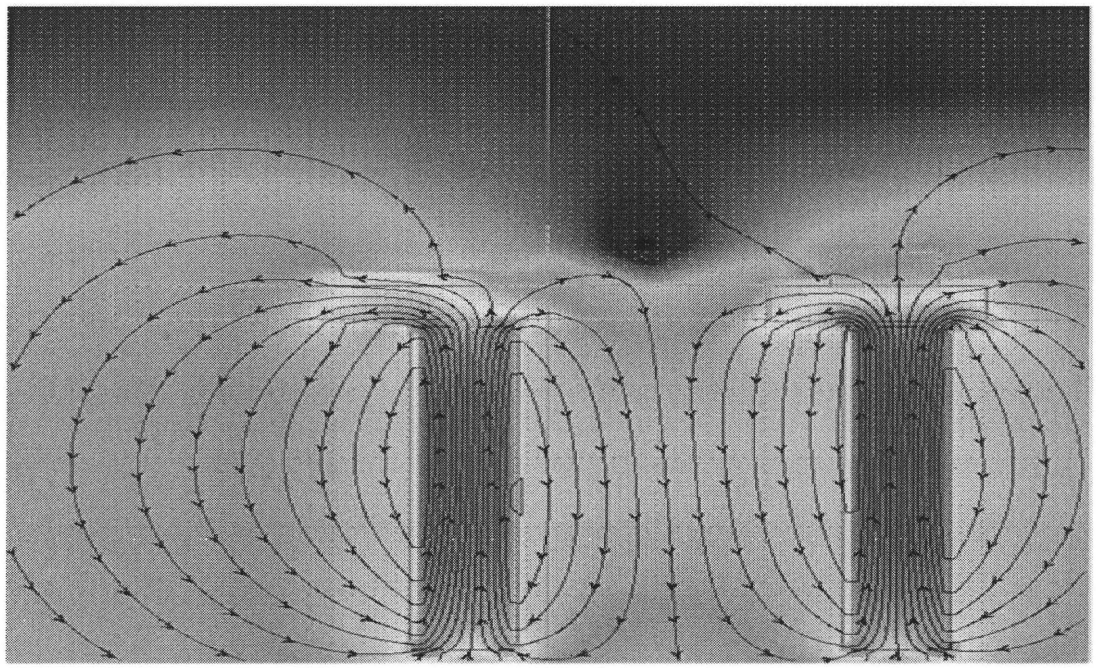

Figure 5.4 b A simulation in which dimensions of air and metal are same and external field sources are moving towards each other;
Case IV; $B_x = 1.33 \times 10^{-9}$ T; $B_y = -5.41 \times 10^{-10}$T; $B = 1.43 \times 10^{-9}$T.

In Table 5.4, the details of the physical dimensions, permeability of the materials and the magnetic strength of the solenoids are presented. The distance between the solenoids is 90 grid units.

Mesh size	1 mm
Dimension Soft magnetic material below the device	9.93 mm by 4.75 mm
Permeability of the soft magnetic material	125
Dimension of the air between the magnetic material	4.97 mm by 20.20 mm
Permeability of air	1
Dimension of Hard magnetic material in the substrate	4.9 mm by 20.20 mm
Permeability of the hard magnetic material (between airs)	125
Dimensions of the magnet	10 mm by 50 mm
Permeability of the magnet	125
Number of turns	100
Current in solenoid	1μamp
Number of magnets	2

Table 5.4: Physical parameters considered when the solenoids are moving towards each other the length of magnetic layer (on the substrate) and the length of the air between the magnetic materials is same. (Case IV)

CHAPTER 6

RESULTS AND DISCUSSION

The results of the simulation of the forces as function of distance, using ViziMag, are summarized in the following section:

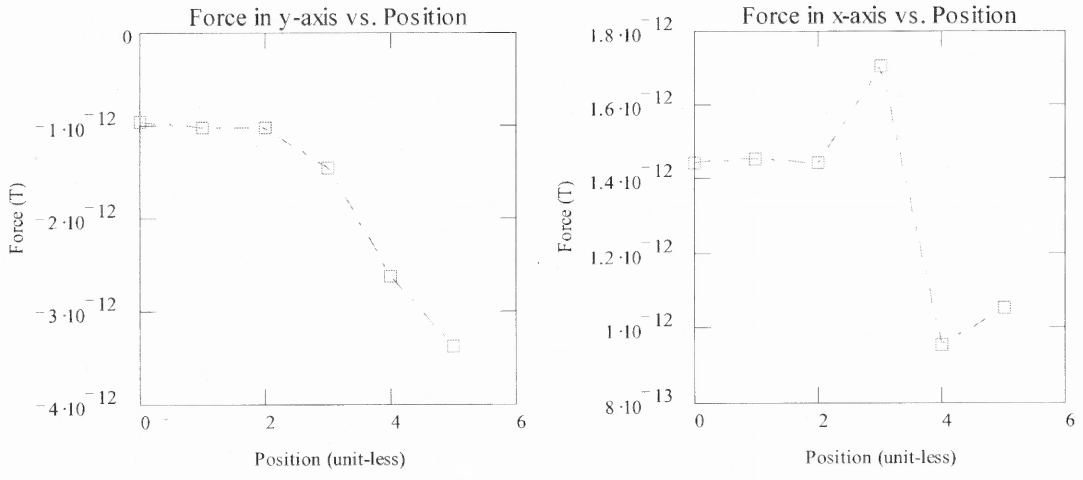

Figure 6.1 (a) Force on device in the vertical plane as function of position of magnet for case I – **(b)** Force on device in the horizontal plane as function of position of magnet for case I. Force (T) is in Newtons and the positions represent number of steps (dimensionless); step size = 10 mm.

Figure 6.1(a) shows a graph between the magnetic force experienced in the y direction on the hard magnetic layer (i.e. the device) and position of the magnet (along a straight path). Similarly, the other graph, Figure 6.1(b), shows a graph of the force experienced in the x direction by the magnetic layer (i.e. the device) as a function of various positions of the magnet. In this simulation, the different layers of the substrate (the magnetic material and the air) are of unequal dimensions and the two solenoids (magnets) move towards each other by 10 mm; i.e., the distance between the solenoids is

90 mm (Figures 5.1a and 5.1b (case I)).

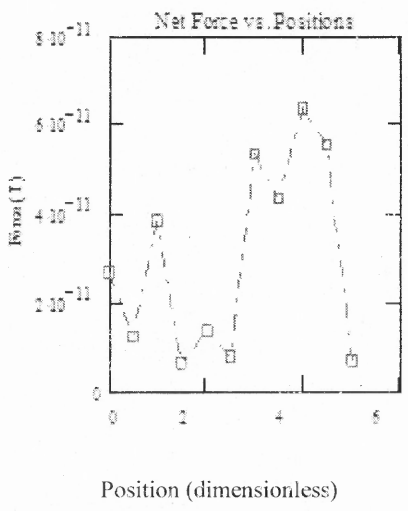

(a)

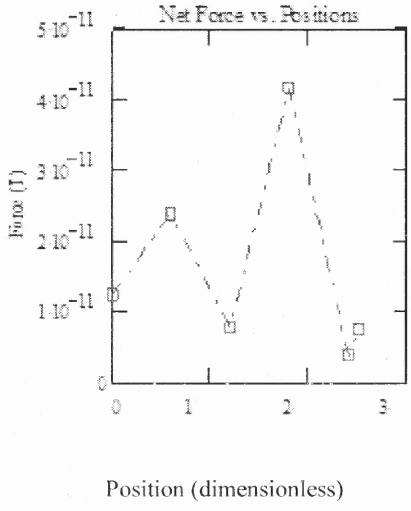

(b)

Figure 6.2 (a) Net force on device as a function of position of device for case II, (a) step size = 6 mm, (b) Net Force on device as a function of position of device for case III, (b) step size = 15 mm. Force (T) is in Newtons and the positions represent number of steps (dimensionless).

Figure 6.2 (a) shows a graph between the net magnetic force experienced by the hard magnetic layer (i.e. the device) and various positions of the device. In this simulation (Figure 6.2a), the width of the recess (magnetic layer) and the spacing between the recesses are of unequal dimensions (case II, Figures 5.2a and 5.2b). Similarly, the other graph, 6.2 (b) shows the net force experienced by the hard magnetic layer (i.e. the device) and different positions of the device (case III). In this simulation (Figure 6.2b), the different layers of the substrate (the magnetic material and the air) are of equal dimensions and the two solenoids (magnets) move towards each other (Figures 5.3a and 5.3b).

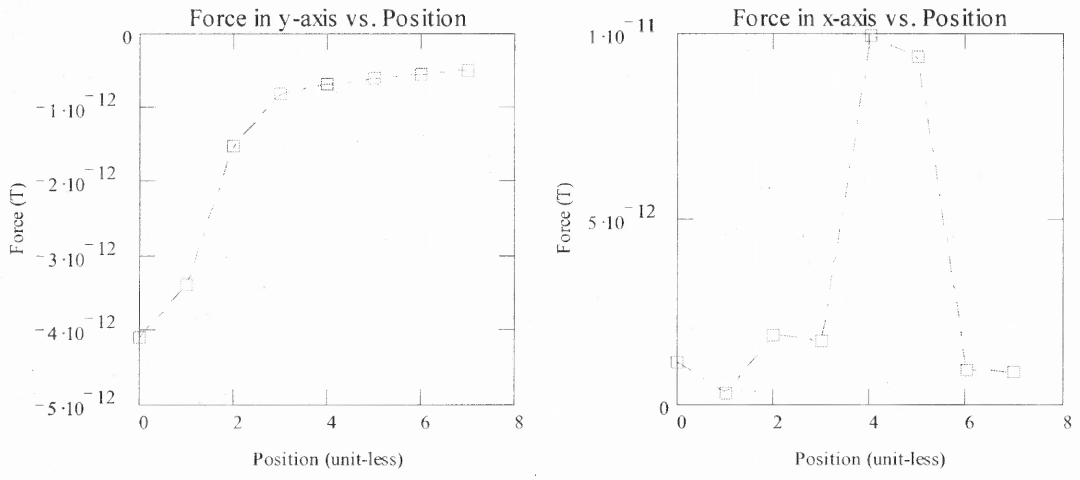

(a) (b)

Figure 6.3 (a) Force on device in the y axis as a function of position of the solenoids (magnets) for case IV; (b) Force on device in the x axis as a function of the position of the solenoids (magnets) for case IV. The dimensions of the recesses (magnetic layer) and the distance between the recesses (air) are the same. Force (T) is in Newtons and the positions represent number of steps (dimensionless); step size = 10 mm.

Figure 6.3 (a) shows a plot of the magnetic force experienced in the y direction on the hard magnetic layer (i.e. the device) versus the various chosen locations of the magnet in relation to its initial position. Similarly, the other graph, Figure 6.3(b), shows the force experienced in the x direction by the magnetic layer (i.e. the device) as a function of different positions of the magnet. In this simulation, the recess and the spacing between the recesses (the magnetic material and the air) are of equal dimensions and the two solenoids (magnets) are moved towards each other - Figures 5.4a and 5.4b (case IV).

In all the above examples, two solenoids of width 10 mm, height 50 mm, and 100 turns each, carrying 1 μamp, with a core of permeability 125 (relative to air of permeability 1), have been considered. The substrate of thickness 5.96 mm exists above the solenoids, and it consists of alternating regions of hard magnetic material with permeability of 125 and non-magnetic material with permeability 1 (air). The horizontal dimensions of the alternating hard magnetic and non-magnetic material are denoted by w_m and w_a mm, and their values differ in the examples presented below. On top of the substrate is a single "device" with soft magnetic layer of permeability 125, width 10.15 mm, and height 3.97 mm. (shown in Figure 5.1(a))

In the set-up for Figure 6.1, the width of the hard magnetic region is w_m =10.04 mm and the width of the non-magnetic region is w_a = 20.20 mm (case I). The x-component of the force acting on the device (right panel, Figure 6.1(b)) shows little variation, initially, with change in distance between solenoids and gradually increases. This is due to the vectorial addition of the force components from both the solenoids. It decreases rapidly and attains a minimum value. This is because of the vectorial subtraction of the force components. The y-component of the force in Figure 6.1(a) (left panel) exhibits a gradual increase with decreasing distance between solenoids. It is to be noted that, in these simulations, the solenoids are being moved towards each other in steps of 10 mm. The downward y-component acting on the device decreases as the distance to the nearest solenoid increases.

Figure 6.2a shows the results of a simulation in which the dimensions w_m (width of the magnetic material in the recess) and w_a (width between the recess i.e. air) are equal and are equal to 10.04 mm. The soft magnetic device stays fixed at an origin, which is

such that the right-hand vertical edge of the device is aligned with the left-hand vertical edge of the left-hand solenoid. See Figure 5.1(a), in which the device is displaced to the right of this position by 6mm. Figure 6.2(a) shows the force acting on the device as it is moved 6 mm towards the right. Similarly, in Figure 6.2(b) the width of the magnetic material inside the recess, w_m and the width between the recesses (air) w_a are of different dimensions and the device is moved to the right in steps of 15 mm. In Figure 6.2(a) (case II), the net force experienced by the device fluctuates as the device is moved along the substrate. As can be seen in Figure 6.2(b), the variation of the net force with position is very similar to that in Figure 6.2(a), but the maximum force experienced by the device is not at the same position because the dimension of w_a and w_m are not the same.

In the set-up for Figure 6.3 (case IV), the width of the hard magnetic region is w_m =20.20 mm and the width of the non-magnetic region is w_a =20.20 mm, while the device and solenoid locations are the same as in the simulation for Figure 6.1 .The x-component of the force acting on the device (right panel) shows a little variation with change in solenoid distance and is consistently smaller than in Figure 6.1 (note the difference in vertical scales of figures). The trend in the y-component of the force in Figure 6.3 (left panel) is opposite to that in Figure 6.1; in this case, the downward y-component acting on the device decreases as the distance to the nearest solenoid increases. In both examples, the y-component of the force is relatively small, of the order of 10^{-12} N, compared with the maximum x-component of the force in Figure 6.3, of 10^{-11}N.

CHAPTER 7

CONCLUSIONS

An overview of the various techniques for assembly of semiconductor devices and structures has been presented. Magnetic field assisted assembly has been proposed as an enabling technology for device integration. Vizimag-2-D, commercial simulation software, has been employed to analyze the magnetic field as a function of position of the device and an applied external field source. Vizimag is easily scalable to include multi magnetic field sources for simultaneous placement of a large number of devices within recesses in the substrate. The obtained resultant force of one device relative to one or two electromagnets is consistent with those in the literature. The results of the simulation show that, as the source of the magnetic field approaches the recess, the resultant magnetic field is higher; the larger the number of magnets, the better is the control and the ability to displace the device in the desired direction. All the simulations have been performed with the assumption that, for a small device with low weight that is moving on a smooth surface, frictional forces are negligible.

ViziMag is a two dimensional software and this limits its ability to estimate actual magnetic fields or forces experienced by the device. The results of ViziMag simulations are confined to situations when the device is stationary.

The results of the simulations in case I and case IV (Figures 6.1 and 6.3) suggest that the forces in the y direction are opposite to each other, when the solenoids are moved towards each other; even the forces in the x direction do not match and they differ by an order of magnitude.

A comparison of the results in Case II and case III, (Figures 6.2 a, 6.2 b) shows similar trends in the variation of net force with distance but the maximum forces experienced by the device are at different positions and the magnitude of the force has the same exponent.

CHAPTER 8

REFERENCES

1 Sudhakar Shet, Vishal R. Mehta, Anthony T. Fiory, Martin P. Lepselter and N.M. Ravindra, The Magnetic Field –Assisted Assembly of Nanoscale miconductor Devices, JOM, 56, 32 (2004).

2 Mindy Simin Teo, Development of Pick and Place Assembly Techniques for Monolithic Optopill Integration, MS Thesis, Electrical Engineering & Computers Science,Massachusetts Institute of Technology, (2005).

3 Qasem Ramadan, Yoon Seung Uk, and Kripesh Vaidyanathan, Large scale Micro Components Assembly Using an External Magnetic Array, Applied Physics Letters, 90, 172502 (2007).

4 Haiqian Zhang, Salah Boussaad, Nguyen Ly, and Nongjian J. Taob, Magnetic Field-Assisted Assembly of Metal/Polymer/Metal Junction Sensors, Applied Physics Letters, 84, 133 (2004).

5 George A. Riley, Introduction to Flip Chip, www.flipchips.com, May (2000).

6 http://www.flipchips.com/tutorial02a.html, May (2000).

7 Laurie S. Roth and Vince Mctaggart of Stud Bump Bonding, http://ap.pennet.com/Articles/Article_Display.cfm?Section=Articles & Subsection=Display & Article_ID=220943, May (2008).

8 Ulrich Kessler, Wolfgang Eberhardt, Adrian Schwenck, Daniel Warkentin, Heinz Kück, Properties of Polymer Bumps for Flip Chip Mounting on Moulded Interconnect devices, Proceedings Electronics System Integration Technology Conference, Dresden, Germany, 288 (2006).

9. His-Jen J. Yeh and John S. Smith, Fludic Self Assembly for the Integration of GaAs Light Emitting Diodes on Silicon Substrates, IEEE Photon.Tech. Lett., 6, 706 (1994).

10. Ashish K. Verma, Mark A. Hadley, Hsi-Jen J. Yeh, and S. Smith, Fluidic Self-Assembly of Silicon Micro Structures, Proc. IEEE, 1263 (1995).

11 J.K. Tu, J.J. Talghader, M.A. Wadley and J.S. Smith of Fluidic self-assembly of InGaAs vertical cavity surface emitting lasers onto silicon,Electronics Letters,31, 1448 (1995).

12 C. G. Fonstad, Jr. and M. Zahn, Method and System for Magnetically Assisted

Statistical Assembly for Wafers, U.S. Patent No. 6888178, May 3 (2005); C. G. Fonstad, Jr., Method and System for Magnetically Assisted Statistical Assembly for Wafers U.S. Patent No. 6825049, Nov 30 (2004).

13 https://dspace.mit.edu/retrieve/3964/AMMNS013.pdf, 22 February (2004).

14 V. Bondarenko, G. Troyanova, M. Balucani and A. Ferrari', Science and Technology of Semiconductors on Insulators, Structures and Devices in Harsh Environment,, Springer (2005);

15 Qasem Ramadan,Yoon Seung Uk, and Kripesh Vaidyanathan, Large scale Micro Components Assembly Using an External Magnetic Array, Applied Physics Letters, 90, 172502 (2007).

16 www.atlassoftware.com, May 22(2008).

17 Rene D. Revero, S. Shet, Michael R. Booty, A.T. Fiory and N. M. Ravindra, Modeling of Magnetic Field Assembly of Semiconductor Devices, Journal of Electronic Materials, 37, 4, 374 (2008).

18 Henrik Jakobsen, Svein Moller Nilsen, Soheil Habibi and Timothy Lommasson, Micro-Electromechanical devices, US Patent No. 6756138, 30 November (2000).

19 Mindy Simi Teo, Development of Pick and Place Technique for Monolithic Optopill Integration, Electrical & Computer Engineering Department, Massachusetts Institute of Technology, January (2005).

20 http://www.g-p-r.com/electric.htm, May (2008).

21 www. jpkc.njust.edu.cn/dxwl/ch16-gauss'law.doc, May (2008).

22 ece-www.colorado.edu/~bart/book/book/chapter4/ch4_6.htm, May (2008).

23 Sudhakar Shet, Rene D. Revero, Michael R. Booty, Anthony T. Fiory, Martin P Lepselter, and Nuggehalli M. Ravindra, Microassembly Techniques: A Review, Proc. Materials Science & Technology, 1, 451, (2006).

24 Timir Datta, Columbia, SC of Gravitational Gauss' Law in the Laboratory: A 21 Century Archimedes problem, 0602163, May (2008).

25 www.lrsm.upenn.edu/~frenchrh/opes.html., May (2008).

26 http://maxwell.byu.edu/~spencerr/websumm122/node70.html., May (2008).

27 Sir Richard Glazebrook, Electricty & Magnetism, An Elementary Textbook, Theoretical and Practical, Phillips Press, New York (2008).

28 J.D. Jackson, Classical Electrodynamics, John Wiley & Sons, New York (1975).

29 Oleg D. Jefimenko, Electricity and Magnetism, 2nd Edition, Appleton-Century-Crofts, Star City (1966).

30 http://www.math-linux.com/spip.phparticle53., May (2008).

31 http://numericalmethods.eng.usf.edu/topics/gaussian_elimination.html, May (2008).

32 www.vizimag.com/tutorial.pdf, May (2008).

33 www.netdenizen.com, May (2008).